

Supplementary Materials for

Computer-Aided Design of Stability Enhanced Nicotinamide Cofactor Biomimetics for Cell-Free Biocatalysis

*Alexandra P. Platt*¹, *Heidi Klem*², *Sam J. B. Mallinson*³, *Yannick J. Bomble*^{3*}, *Robert S. Paton*^{1*}

¹Department of Chemistry, Colorado State University, Fort Collins, CO, 80523, USA

²Thermodynamics Research Center, Applied Chemicals and Materials Division, National Institute of Standards and Technology, Boulder, CO, 80305, USA

³Biosciences Center, National Renewable Energy Laboratory, Golden, CO, 80401, USA

*Corresponding e-mail: yannick.bomble@nrel.gov, robert.paton@colostate.edu

Table of Contents

1 NCB Generation Protocol	S2
2 Experimental Stability Data for Comparison	S8
3 Representing NCB Stability	S8
4 Conformational Sampling Protocol	S13
4.1 Ground State Structure Conformational Sampling.....	S13
4.2 Transition State Structure Conformational Sampling	S14
5 Quantum Mechanical (QM) Calculation Details	S15
5.1 Geometry Optimization and Vibrational Frequencies	S15
5.2 Single Point Energy Corrections.....	S16
6 High-Throughput Calculation Details	S18
6.1 Key Atom Determination.....	S18
6.2 Natural Bonding Orbital Partial Charge Calculations	S18
6.3 Fukui Index Calculations.....	S19

6.4 Semi-Empirical Descriptor Calculation.....	S20
7 Predictive Modeling of NCB Stability with ROBERT.....	S24
8 Mean Stabilities of Each Substituent	S32
9 Generation and Testing of Out-of-Sample NCBs	S33
References.....	S36

1 NCB Generation Protocol

Structures for the novel nicotinamide cofactor biomimetics (NCBs) studied in this work were created systematically using RDKit version 2022.02.2¹ with Python 3.9.7. The pyridinium core present in the oxidized cofactors was created from SMARTS. We also generated possible R₁, R₂, and R₃ substituents as lists of SMILES representations to add to the core. The substituents were combinatorically added to the pyridinium core at each designated position to create 132 distinct NCBs.

We then performed further “reactions” in RDKit to reach the reduced, or 1,4-dihydropyridine, forms of the cofactors, which were the forms primarily studied in this work (Figure S1). This was done by altering the bond types and atomic charges, as well as adding explicit hydrogen atoms where necessary to the core structure of the NCBs to reach the final desired structure. We followed a similar procedure to generate degraded forms, analogous to Int I (Figure 4 in the main text). To finally create the library of NCB structures, all molecules created in RDKit were saved as SMILES representations to be used for the remainder of this work.

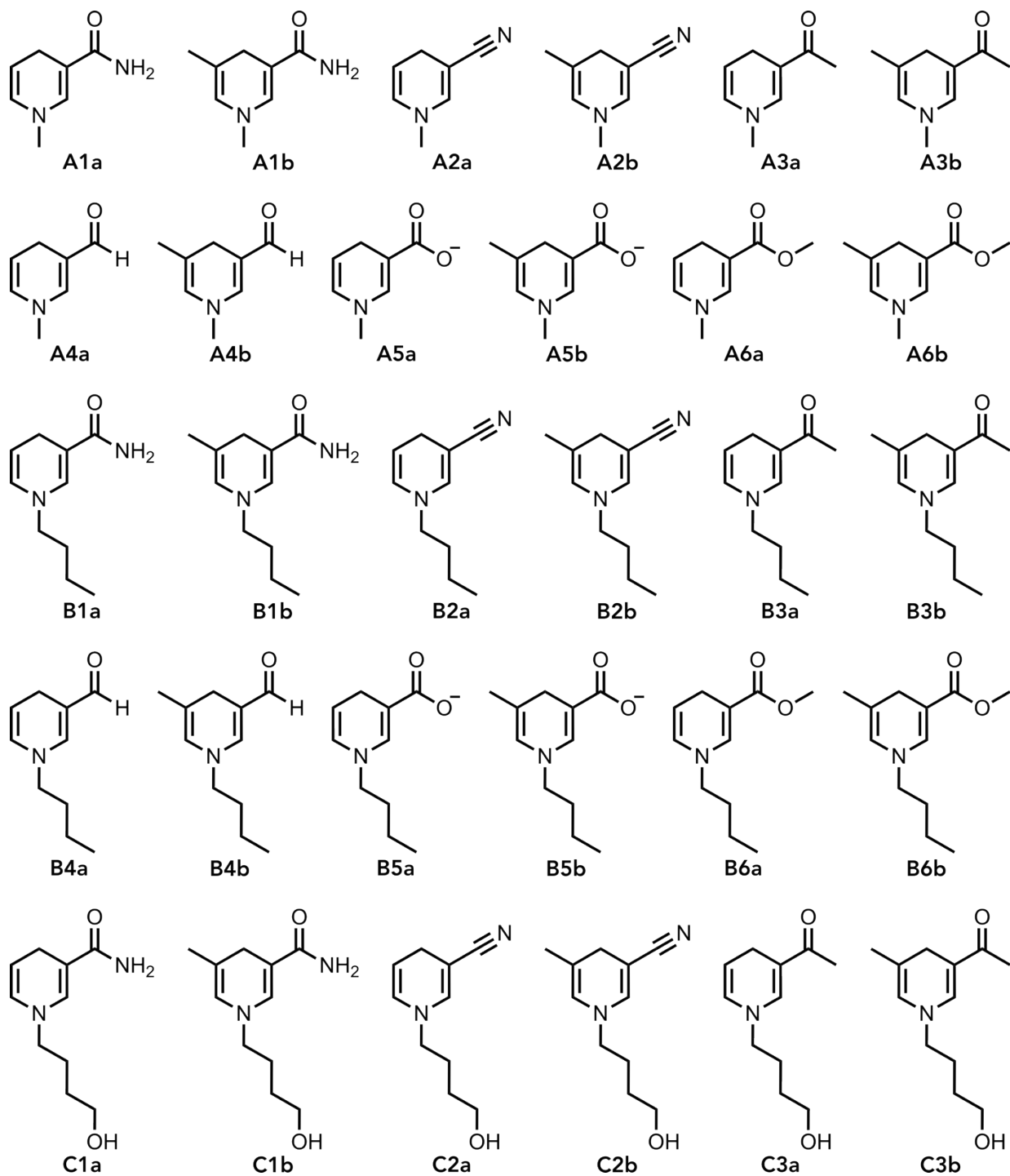


Figure S1. Structures of each reduced NCB in our library, labeled based on substituent identity.

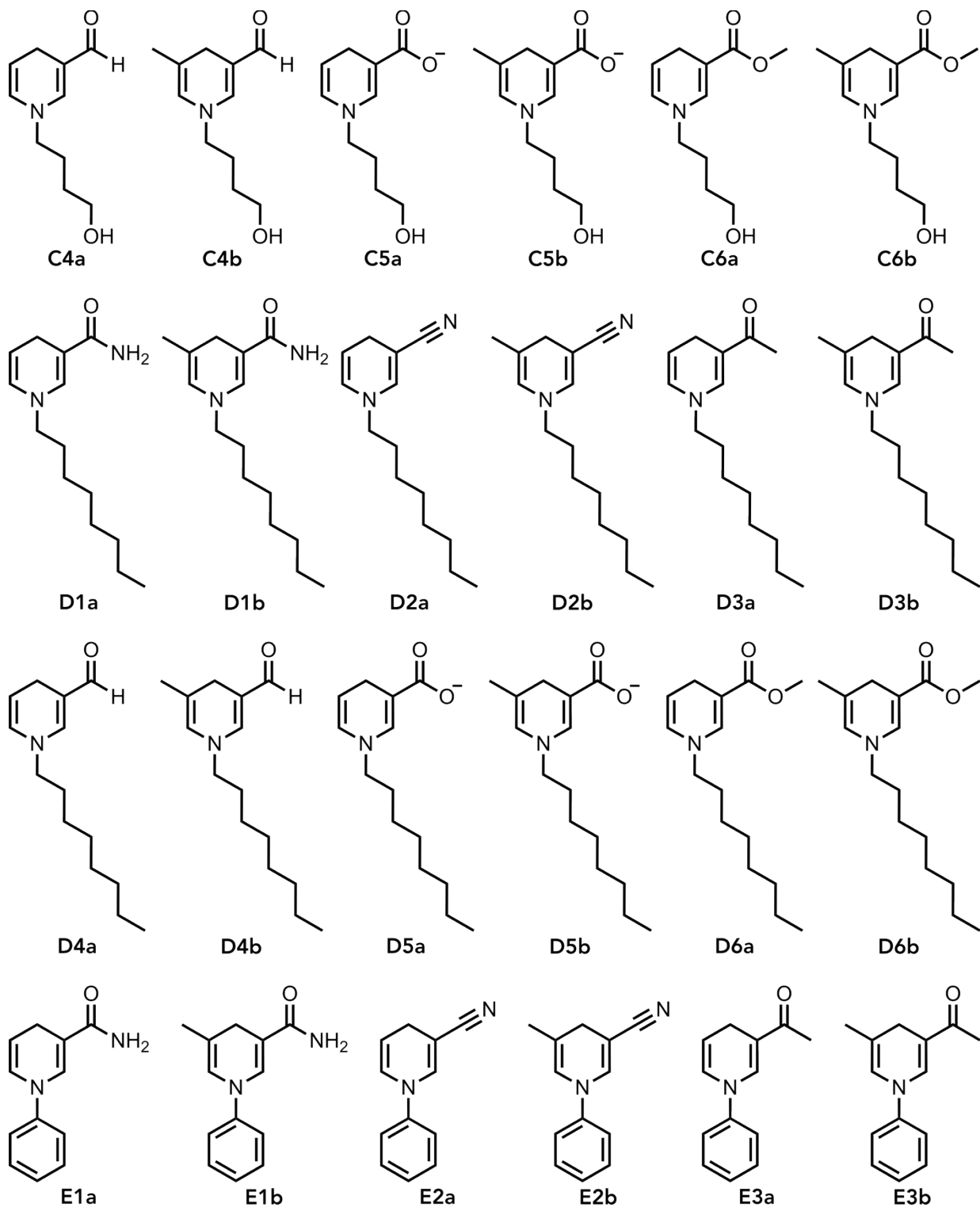


Figure S1 cont. Structures of each reduced NCB in our library, labeled based on substituent identity.

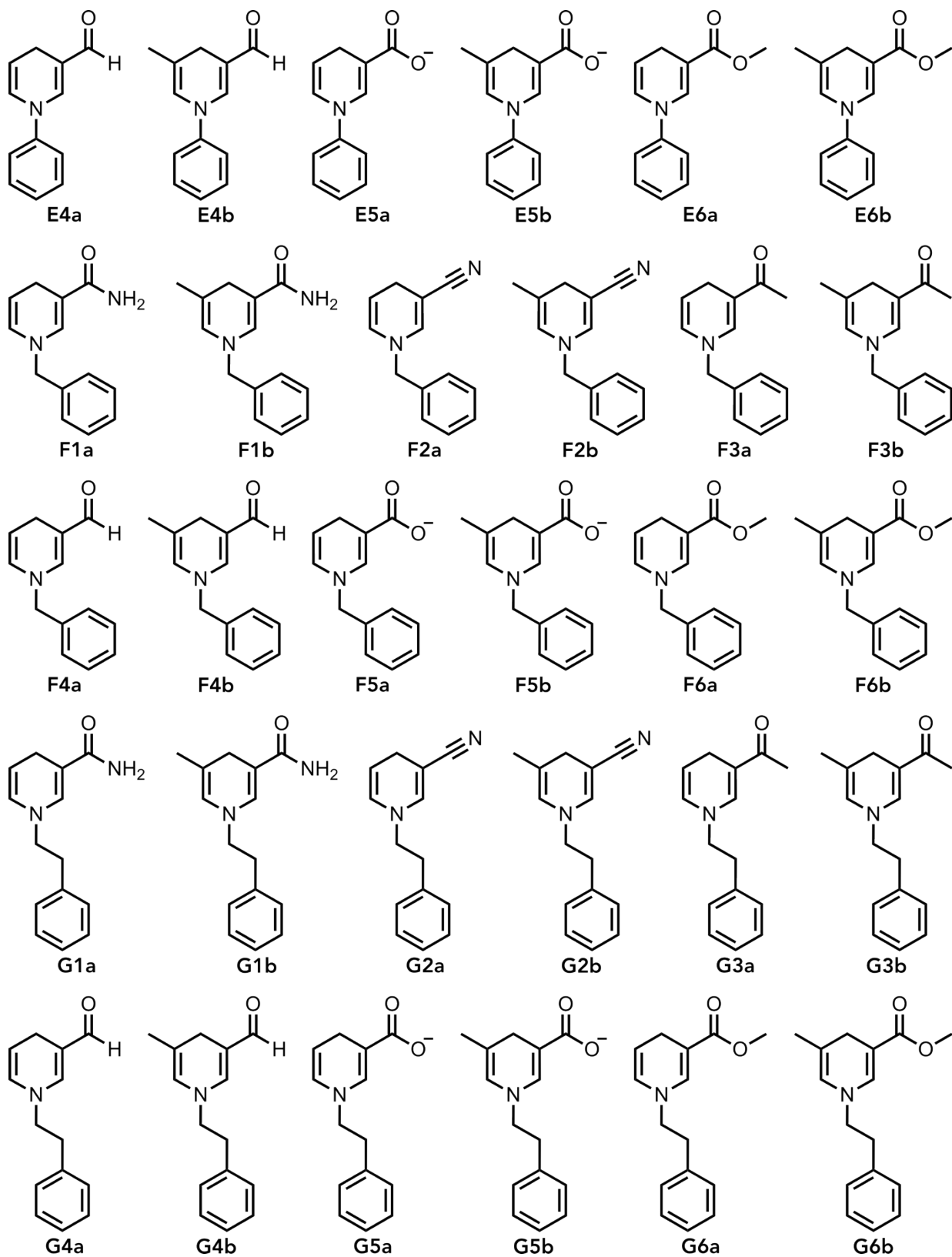


Figure S1 cont. Structures of each reduced NCB in our library, labeled based on substituent identity.

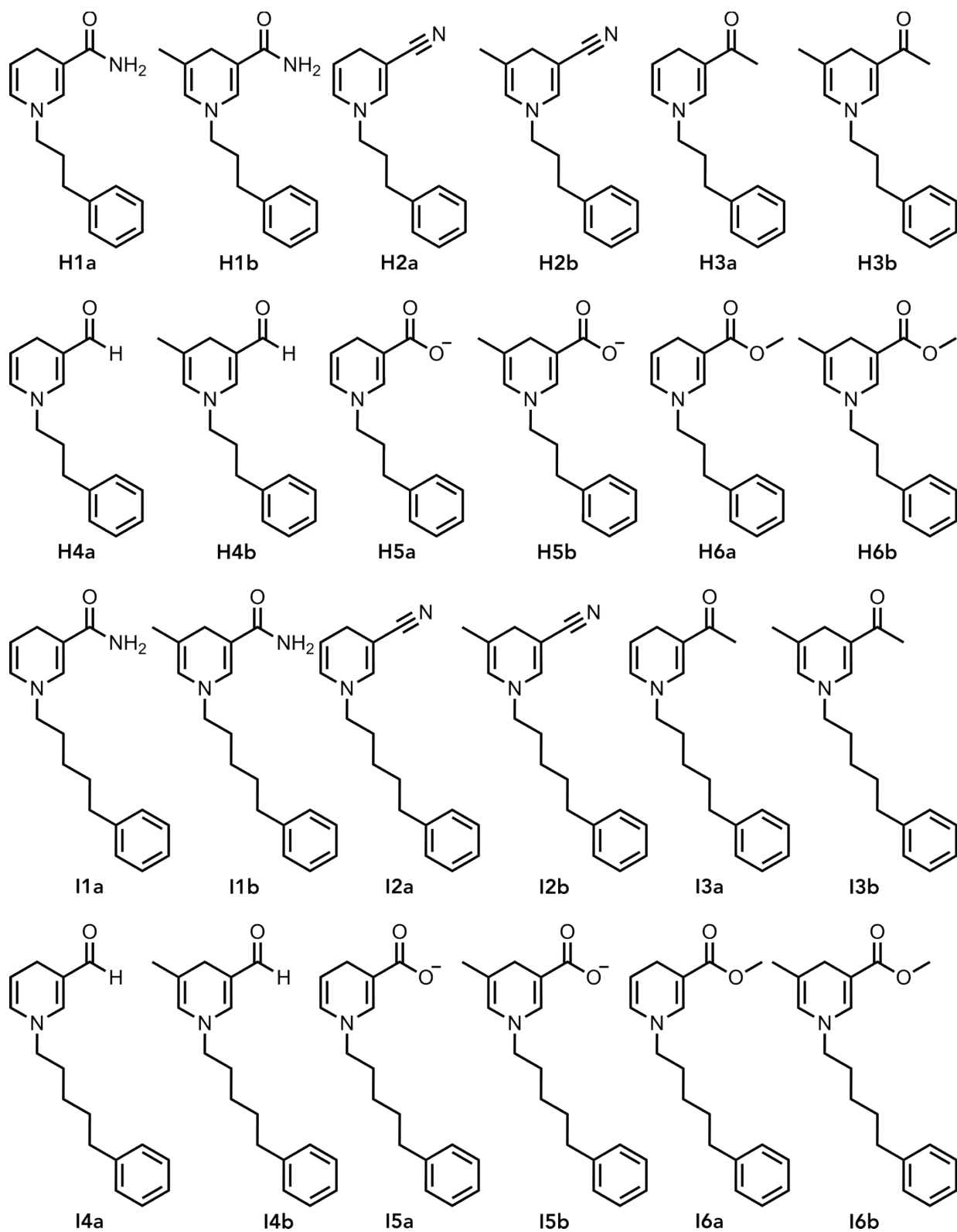


Figure S1 cont. Structures of each reduced NCB in our library, labeled based on substituent identity.

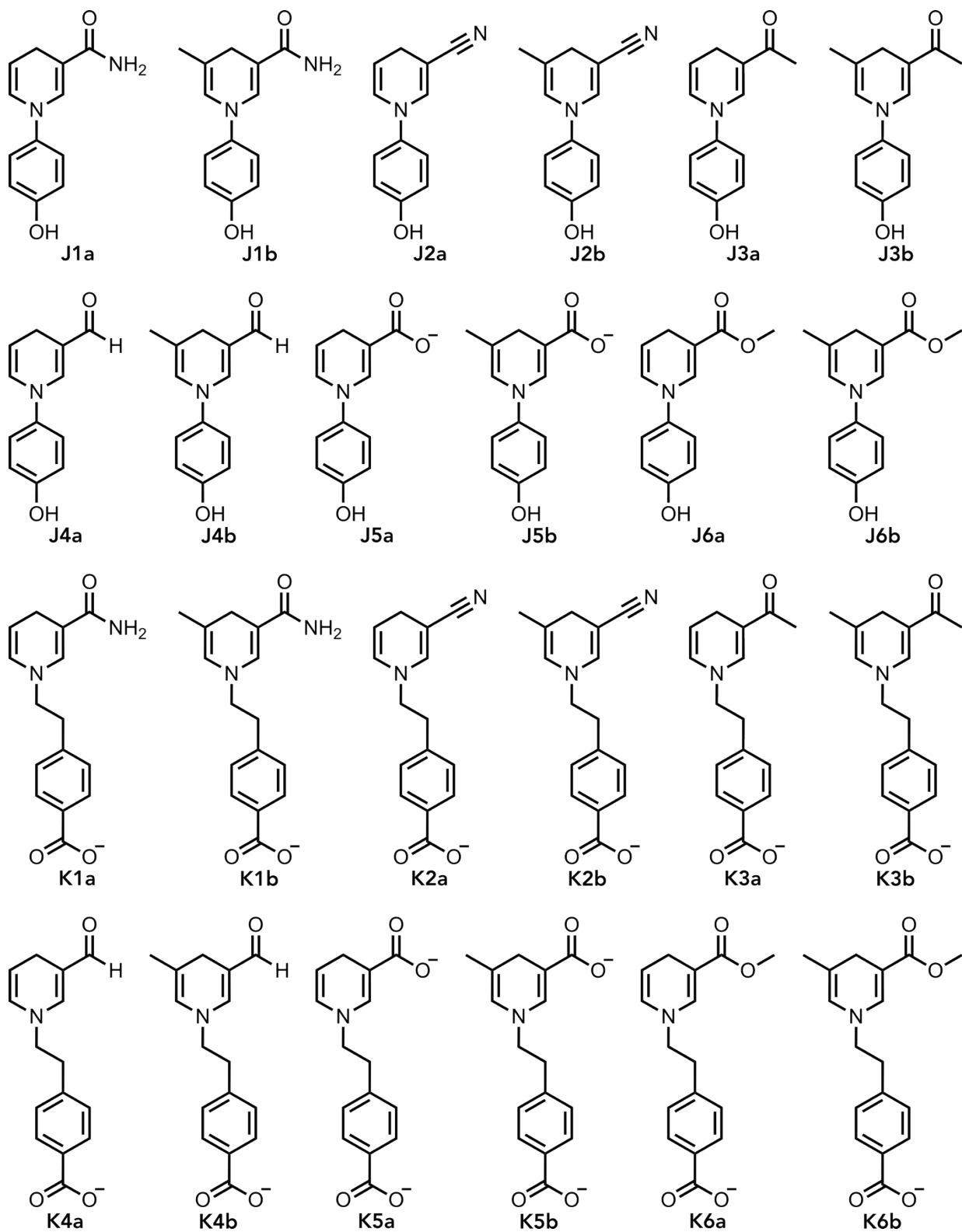


Figure S1 cont. Structures of each reduced NCB in our library, labeled based on substituent identity.

Using the SMILES representations of our NCB library, we then used OpenBabel version 3.1.1² to convert the SMILES representation into an xyz-coordinate file of each structure. Then, all structures underwent the conformation sampling protocol as detailed above before density functional theory (DFT) geometry optimization, vibrational frequency calculations, and single-point energy corrections. The QPREP and QCORR modules of AQME version 1.5.1³ were used to create DFT input files and ensure that all DFT computations finished properly.

2 Experimental Stability Data for Comparison

Experimental barriers were calculated from reported rate constants for the decomposition of NCBs in 0.1 M potassium phosphate buffer at pH 7.⁴ These effective rate constants were converted to reaction barrier heights with the Eyring equation:

$$k = K \frac{k_B T}{h} e^{\frac{-\Delta G^\ddagger}{RT}}$$

where k_B is the Boltzmann constant, T is the temperature of the system (298.15 K), h is Planck's constant, R is the gas constant, ΔG^\ddagger is the energy barrier for the reaction, K is the transmission coefficient (1.0), and k is the rate constant, calculated by:

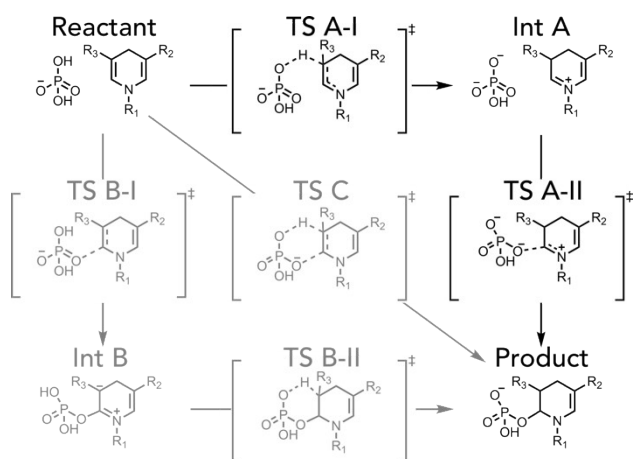
$$k = \frac{k'}{0.1 \text{ M}}$$

where k' is the effective rate constant reported in literature and 0.1 M is the concentration of potassium phosphate buffer. Using these equations, we were able to convert reported rate constants into reaction free energy barriers and compare with our computed DFT barrier values.

3 Representing NCB Stability

This work examined three possible degradation pathways based on the proposed mechanism by Alivisatos et al. (Scheme S1).⁵ This reaction could occur in a stepwise manner, beginning with a proton transfer to the C5 carbon followed by C–O bond formation between phosphate at the C6 carbon (Pathway A). These steps could also occur in the reverse order (Pathway B). Degradation could also be a concerted process, where both events happen simultaneously (Pathway C). Pathway A is the most likely pathway for NCB degradation according to our DFT studies. Geometry

optimizations of Int B naturally relaxed to the reactant or product species, likely due to instability of the carbanion formed at the C5 carbon. Thus, pathway B was not a reasonable pathway for NCB degradation to follow. Similarly, TS C could not be isolated, instead relaxing to TS A-I or A-II.



Scheme S1. Possible degradation pathways for NCBs. Pathway A (black) is followed, starting with a proton transfer to C5 followed by a C–O bond formation at C6.

The results of our mechanistic study show that these 4 NCBs behave similarly, showing the same patterns of degradation (Figure S2). Each NCB degradation pathway shows TS A-I is higher in energy than TS A-II, so the first step of degradation is key. Additionally, since each NCB degradation pathway follows the same trend, this is likely to translate to other NCBs for which we do not have experimental degradation barrier. In this study, the reactants were optimized at infinite separation, while Int A was treated as a complex. The structures for the complexes were optimized from the appropriate endpoint of the intrinsic reaction coordinate (IRC) pathway from each transition state.

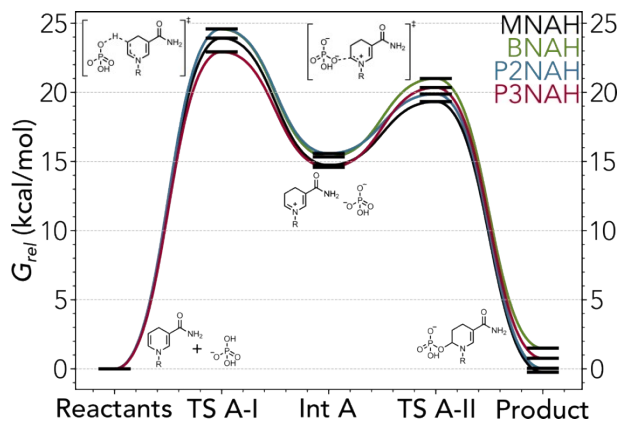


Figure S2. Potential energy surface showing the degradation reaction for 4 sample NCBs. DFT calculations were done using ω B97M-V/def2-TZVP/SMD(water)//PBE0-D3(BJ)/6-31+G(d)/SMD(water).⁶⁻²⁹

Because the high-energy first step of degradation (TS A-I) is key to degradation, it reasons that the kinetic barrier of TS A-I (ΔG^\ddagger) is an appropriate measure of stability. However, finding the transition state structures necessary to obtain this kinetic information is time consuming and costly, making this stability metric not feasible for a high-throughput study. Thus, we turned to the free energy difference between Int A and the reactants (ΔG).

To ensure using ΔG to represent stability is acceptable for our NCB library, we measured the correlation between ΔG and ΔG^\ddagger for a representative subset of our library (Table S1). These 34 structures were selected using a binning procedure based on the $f(-)$ value for the C3 atom, the first atom of the R_2 substituent (that bound to the C3 carbon), and the C4 hydrogens (C4H), as well as NBO partial charges at the C2, C3, C5, N1, and C4H atoms (Figure S3). These NCB features were chosen as they are shown to be important to NCB stability. We used 2 bins for each of the 8 descriptors and sampled uniformly from them. The NCBs selected for this analysis were: **A1a**, **A3b**, **A5a**, **A5b**, **B2b**, **B3a**, **B6b**, **C1b**, **C3b**, **C6a**, **D3a**, **D5b**, **D6a**, **E1a**, **E1b**, **E2a**, **E2b**, **E3a**, **E3b**, **F1a**, **F3b**, **G3b**, **G4a**, **J1a**, **J1b**, **J4a**, **J5a**, **J5b**, **J6a**, **K1b**, **K3a**, **K3b**, **K4b**, and **K6b**.

Table S1. Values of ΔG and ΔG^\ddagger for a representative subset of our expanded NCB library. ΔG values are at PBE0-D3(BJ)/def2-TZVP/SMD(water)//PBE0-D3(BJ)/6-31+G(d)/SMD(water). ΔG^\ddagger values are at ω B97M-V/def2-TZVP/SMD(water)//PBE0-D3(BJ)/6-31+G(d)/SMD(water).

<i>NCB</i>	ΔG (kcal/mol)	ΔG^\ddagger (kcal/mol)
A1a	-134.7	22.2
A3b	-128.2	26.6
A5a	-140.9	19.5
A5b	-137.8	21.6
B2b	-128.2	25.8
B3a	-133.1	22.3
B6b	-129.9	24.8
C1b	130.1	23.6
C3b	-127.9	27.0
C6a	-132.3	22.8
D3a	-132.2	26.1
D5b	-138.4	22.4
D6a	-133.1	23.7
E1a	-129.4	24.6
E1b	-126.1	27.1
E2a	-125.9	26.7
E2b	-122.8	29.0
E3a	-127.5	25.4
E3b	-124.9	27.0
F1a	-133.3	23.3
F3b	-128.4	26.0
F6a	-131.5	24.9
G3b	-129.0	25.5
G4a	-126.7	26.4
J1a	-130.7	24.6
J1b	-127.0	27.0
J4a	-124.4	30.7
J5a	-136.0	21.7
J5b	-133.2	22.8

K1b	-129.7	24.6
K3a	-132.1	25.6
K3b	-128.5	26.1
K4b	-124.6	27.5
K6b	-129.9	26.0

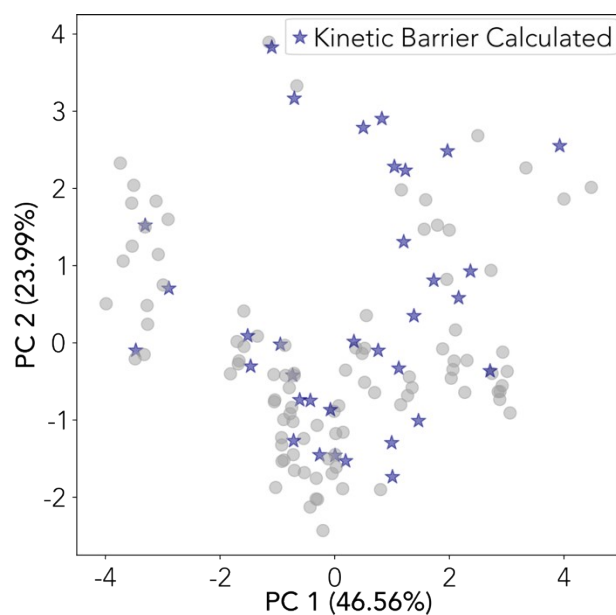


Figure S3. Principal component analysis (PCA) showing the NCB scope of this study with structures used to determine the correlation between ΔG and ΔG^\ddagger shown as blue stars.

After determining a stability metric that works for our system, we were also able to examine the stability of our library relative to a mononucleotide biomimetic cofactor, nicotinamide mononucleotide (NMNH⁻). This cofactor, with a stability of -134.1 kcal/mol, was among the less stable in our library (Figure S4).

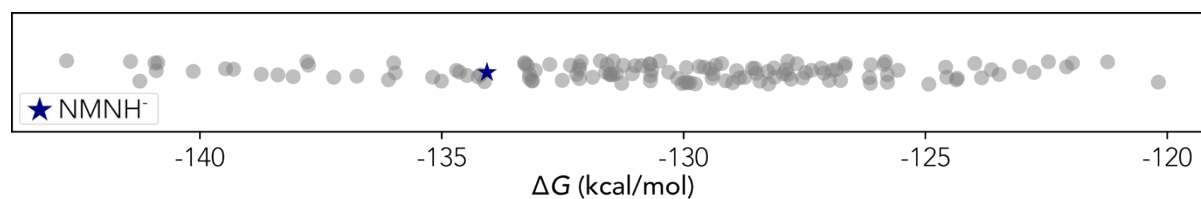


Figure S4. Representation of the stability (ΔG) of the NCBs in our library (grey) compared to that of NMNH⁻ (blue star). Less negative ΔG values indicate higher NCB stability.

4 Conformational Sampling Protocol

Conformational sampling was performed using the Conformer-Rotamer Ensemble Sampling Tool (CREST), version 3.0^{30,31} using the GFN-FF force field³² and the GFN2-xTB³³ semi-empirical level of theory through xTB version 6.7.0.³⁴

4.1 Ground State Structure Conformational Sampling

Ground-state structural conformations were sampled without any constraints, starting from SMILES strings of the molecules and converting to xyz coordinate files with the use of Open Babel version 3.1.1² before performing a CREST conformation search on the structures. Default settings were used except altering the energy window from 6 kcal/mol to 12 kcal/mol to obtain a broad range of structures in the initial conformational sampling. Following the initial CREST search, the CREGEN module was used to filter duplicate structures and those too high in energy. This reduction of sample space was done using CREGEN default settings aside from the duplicate energy threshold (0.1 kcal/mol), the root mean square deviation threshold (0.125 Å), and the lower bound threshold for the rotational constant between molecules (0.1).

Using the ensemble output from CREGEN, we then used Commandline Energetic Sorting (CENSO) version 1.2.0³⁵ to further refine the conformational ensemble for each ground-state structure. Orca version 5.0.3³⁶ was used for low-level DFT single point energy calculations within CENSO used to refine the ensembles. Only Part 0 and Part 1 were used in this study. Part 0, the cheap prescreening, calculated conformer energies at the B97-3C/def2-mTZVP level of theory.^{37,38} Structures more than 6 kcal/mol higher in energy than the lowest energy structure were filtered out of the ensemble at this point. Next, Part 1, prescreening, calculated single point energies of the remaining conformers at the r²SCAN-3c/def2-mTZVPP level of theory.³⁸ Modified rigid-rotor-harmonic-oscillator approximation (mRRHO) contributions were calculated using at the GFN2 level with a constraint to input geometry. Structures more than 4 kcal/mol higher in energy than the lowest energy structure were filtered out of the structural ensembles at this point. No solvent effects were considered when using CENSO.

Following CENSO calculations, each conformational ensemble was then clustered into 10 representative structures based on dihedral angles using principal component analysis (PCA) and k-Means clustering in the CREGEN module of CREST. The final number of structures for this clustering was selected to be 10 due to the range of energies from DFT-optimized structures, as well as the ability to capture multiple low-energy conformation in a sample structure, **C1a** (BuOHNAH), compared with clustering to 5, 10, 15, and 20 structures (Figure S5). All calculations associated with conformational sampling of ground-state structures were done at 298.15 K.

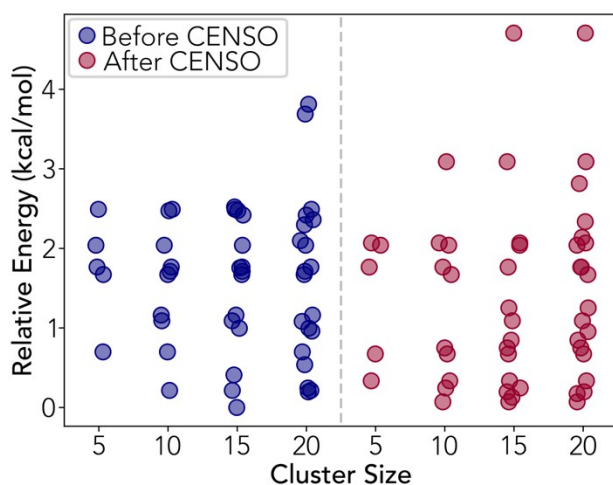


Figure S5. DFT-optimized energies of structural ensembles of sample NCB **C1a**. This analysis was performed by clustering before (blue, left) and after (red, right) the use of CENSO ensemble refinement. DFT was performed at PBE0-D3(BJ)/6-31+G(d)/SMD(water).^{6-15,19,20,25-28}

4.2 Transition State Structure Conformational Sampling

Transition state structures underwent conformational sampling using a similar procedure. First, constrained CREST calculations using a force constant of 1.0 Hartree/Bohr² were run to sample conformational space without losing the transition state structure. For all structures representing TS A-I, constraints were placed on the C5–H, O1–H, and O2–C6 bond distances. Structures representing TS A-II included constraints on the O2–C6 bond distance. Other intramolecular constraints not involved in the transitions state were added as needed to ensure the final ensembles represented the correct transition state. For example, the C–H bonds at the C4 carbon and all P–O bonds were fixed to maintain connectivity.

After the initial CREST conformer search (performed with default settings), the CREGEN module of CREST was utilized to cluster the transition state structural conformers into 10 (or fewer) representative structures. These clustered structures underwent a constrained geometry optimization in Gaussian 16, Revision C.01³⁹ with the same constraints used during CREST. Finally, unrestrained transition state geometry optimizations were performed to give a conformational ensemble of transition state structures.

After visual inspection of the 4 NCBs in the mechanistic study, it was determined that this process was to be repeated. The initial sample did not include the dihedral angle N–C3–C4–C5 at both $\sim 0^\circ$ and $\sim 180^\circ$, so a search was started with each angle to ensure a representative ensemble. This analysis was not deemed necessary for high-throughput analysis of transition state structures or for any ground state structures.

5 Quantum Mechanical (QM) Calculation Details

5.1 Geometry Optimization and Vibrational Frequencies

All geometry optimizations and vibrational frequency calculations in this work were performed at the PBE0-D3(BJ)/6-31+G(d)/SMD(water) level of theory^{6-15,19,20,25-28} using Gaussian 16, Revision C.01.³⁹ The basis set used, 6-31+G(d), included diffuse functions which helped accurately model the negatively charged buffer and cofactors. This basis set is also common for these types of systems and was deemed appropriate for this work. Water was chosen as the solvent for optimization because the experimental barriers that we are comparing our results with were obtained using a 0.1 M solution of buffer, thus the reaction solution was primarily water.

After geometry optimizations, vibrational frequency calculations were performed to determine the nature of all structures. Transition state structures were examined to ensure there was one and only one imaginary vibrational frequency mode. The identity of each transition state was also verified through IRC calculations. Ground state structures had no imaginary vibrational modes.

We performed benchmarking of different functionals to ensure that we were using an appropriate level of theory in this study. To ensure high quality results, we selected three different functionals

to benchmark our results: M06-2X(D3),^{20,40} PBE0-D3(BJ),^{19,20,25–27} and PW6B95-D3(BJ).^{19,20,41} We optimized the reactants, TS A-I, and TS A-II for this benchmarking study. By comparing the barriers of each step with experimental stability data, we were able to determine the best functional to use for our system (Table S2). Based on these data, we selected PBE0-D3(BJ) as the functional which performs best for this system due to the low energy barriers. Energy barriers increased for all functionals after single point energy corrections using a larger basis set, so the lowest energy barriers after optimization signified the best functional to use for this work.

Table S2. Energy barriers for the degradation of sample NCBs optimized with various functionals using the 6-31+G(d) basis set and SMD solvation in water.

<i>NCB</i>	<i>Functional</i>	<i>TS A-I Barrier (kcal/mol)</i>	<i>TS A-II Barrier (kcal/mol)</i>	<i>Experimental Barrier (kcal/mol)^a</i>
A1a (MNAH)	PBE0-D3(BJ)	19.5	15.6	21.1
	M06-2X(D3)	21.6	16.0	
	PW6B95-D3(BJ)	21.9	15.4	
F1a (BNAH)	PBE0-D3(BJ)	19.9	16.6	21.6
	M06-2X(D3)	23.0	18.7	
	PW6B95-D3(BJ)	22.7	16.3	
G1a (P2NAH)	PBE0-D3(BJ)	19.1	15.7	21.6
	M06-2X(D3)	22.6	17.4	
	PW6B95-D3(BJ)	21.7	15.9	
H1a (P3NAH)	PBE0-D3(BJ)	18.0	17.4	21.1
	M06-2X(D3)	21.3	18.8	
	PW6B95-D3(BJ)	20.4	16.2	

^aExperimental values calculated from Nowak et. al, 2017.⁴

5.2 Single Point Energy Corrections

To obtain more accurate energy barriers, additional single point energy corrections were performed on all structures. These calculations were performed using Orca version 5.0.3 built with support for libXC version 5.1.0.^{21,36,42–44,46,47} Structures obtained from lower-level geometry optimization calculations were used as a starting point, then energies were recalculated at a higher level of

theory to obtain more accurate energy values. For this work, we used the larger def2-TZVP basis set²¹⁻²⁴ for these single point energy corrections. Additionally, we tested various functionals for these single point energy corrections. The functionals examined for energy corrections were PBE0-D3(BJ), ω B97M-V,²⁹ and M06-2X(D3) (Table S3).

Table S3. Energy barriers for the degradation of sample NCBs with single point energy corrections calculated at various functionals using the def2-TZVP basis set and SMD water solvation after optimization at PBE0-D3(BJ)/6-31+G(d)/SMD(water).

<i>NCB</i>	<i>Functional</i>	<i>TS A-I Barrier (kcal/mol)</i>	<i>TS A-II Barrier (kcal/mol)</i>	<i>Experimental Barrier (kcal/mol)^a</i>
MNAH	PBE0-D3(BJ)	22.4	19.8	21.1
	M06-2X(D3)	25.1	19.4	
	ω B97M-V	23.9	19.3	
BNAH	PBE0-D3(BJ)	23.0	22.6	21.6
	M06-2X(D3)	26.3	23.9	
	ω B97M-V	24.6	21.0	
P2NAH	PBE0-D3(BJ)	22.3	21.6	21.6
	M06-2X(D3)	26.0	21.7	
	ω B97M-V	24.6	19.6	
P3NAH	PBE0-D3(BJ)	21.3	22.6	21.1
	M06-2X(D3)	24.1	22.1	
	ω B97M-V	22.9	20.3	

^aExperimental values calculated from Nowak et. al, 2017.⁴

Based on these data, we selected the ω B97M-V functional to use for single point energy corrections for the mechanistic study portion of this work. The absolute errors relative to experimental values is slightly higher than with PBE0-D3(BJ), but all values using ω B97M-V are within DFT uncertainty levels (~ 3 kcal/mol),⁴⁷ and the trend is more consistent with experimental results. The barriers for **F1a** and **G1a** are identical in the calculations with ω B97M-V and the barrier heights for **A1a** and **H1a** are also similar. This trend is apparent in the experimental results, suggesting ω B97M-V is the best functional for our system. Due to the limited availability of

experimental stability values and complexity of the system, following experimental trends the most important comparison to ensure for accurate DFT modeling.

While ω B97M-V was determined to be the most accurate functional for energy corrections during mechanistic modeling, we made the decision to perform single point corrections at the PBE0-D3(BJ)/def2-TZVP/SMD(water) level of theory during high-throughput analysis due to computational cost. The functional ω B97M-V is too expensive and time-consuming to realistically use for the high throughput study, which includes over 2,000 structures. Thus, we chose to continue with the PBE0-D3(BJ) functional to find ΔG and calculate DFT-level descriptors. Calculations of ΔG^\ddagger were still done using the functional ω B97M-V because of the small subset of structures.

6 High-Throughput Calculation Details

6.1 Key Atom Determination

There were 10 atoms which were determined to be key, shared atoms between all NCBs in our library: all 6 atoms within the core ring of the cofactor (N1, C2, C3, C4, C5, and C6), the first atom bound to the ring of the R₁, R₂, and R₃ substituents (R₁, R₂, and R₃, respectively), and the mean value for the two H atoms at the C4 position (C4H). Key atom indices were isolated using SMARTS substructure matching of the 1,4-dihydropyridine core in RDKit. The indices of key atoms for each NCB in the library can be found at https://github.com/aplatt22/ncb_stability.

6.2 Natural Bonding Orbital Partial Charge Calculations

Natural bonding orbital (NBO) charges were calculated for the reduced structures of all NCBs. These calculations were done using NBO version 7.0.5⁴⁸ to calculate the partial charges on key atoms of the reduced NCB species at the PBE0-D3(BJ)/def2-TZVP/SMD(water)//PBE0-D3(BJ)/6-31+G(d)/SMD(water) level of theory. Partial charges at only the 10 key atoms were used as descriptors for predictive modeling.

NBO partial charges at select atoms demonstrated a categorical nature (Figure S6). Thus, it was not necessary to include steric descriptors as part of the DFT-level dataset. The NBO partial charge

of the C5 carbon is a prime example of this behavior, displaying a bimodal distribution corresponding to the identity of the R₃ substituent.

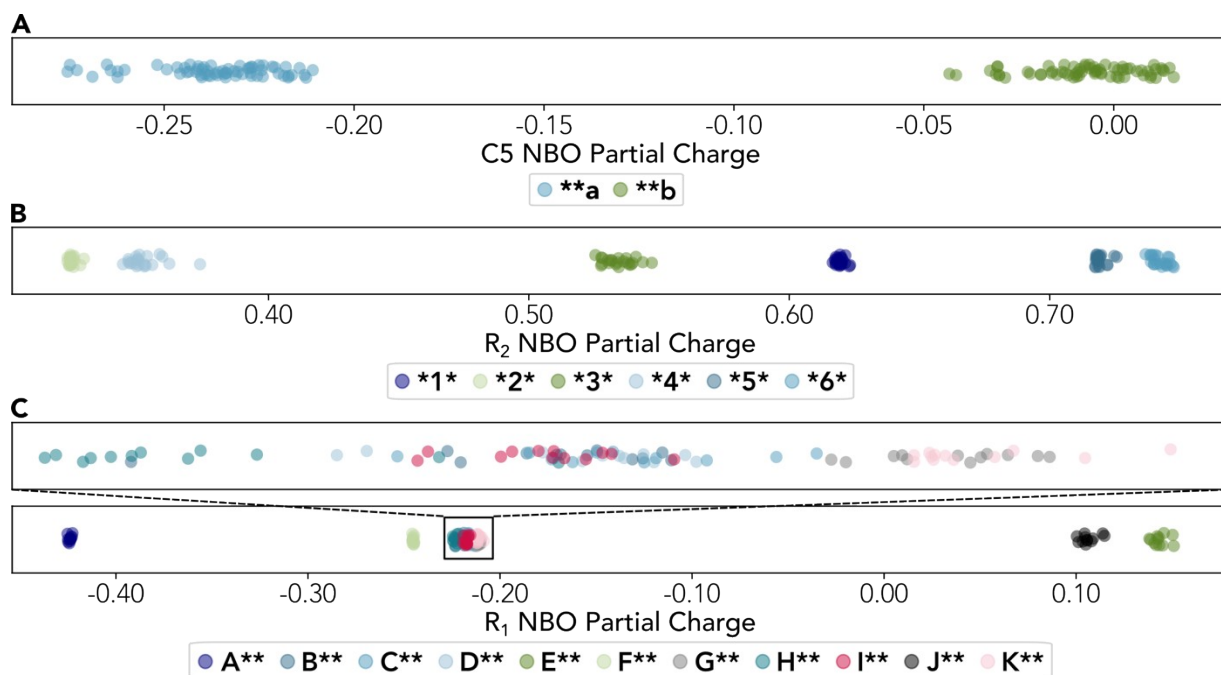


Figure S6. Representation of select NBO partial charges of NCBs within our virtual library. These features of the NCBs demonstrate a somewhat categorical nature, eliminating the need for steric descriptors when training predictive models for NCB stability.

6.3 Fukui Index Calculations

Electrophilic ($f(-)$) and nucleophilic ($f(+)$) Fukui indices⁴⁹ were calculated from optimized geometries, adjusting the charge and multiplicity to reflect the addition or removal of a single electron, respectively. Structures were not reoptimized using these updated charges and multiplicities. The NBO partial charges for these species were calculated with NBO version 7.0.5.

⁴⁸ An in-house python script was then used to extract the partial charges at each atom and calculate $f(+)$ and $f(-)$ following:

$$f(+) = P(n+1) - P(n)$$

and

$$f(-) = P(n) - P(n-1)$$

where $P(n)$ is the NBO partial charge of an atom of the original structure, $P(n+1)$ is the NBO partial charge of the atom after the addition of one electron, and $P(n-1)$ is the NBO partial charge of the atom after the subtraction of one electron. Fukui indices were only isolated for key atoms.

6.4 Semi-Empirical Descriptor Calculation

In addition to calculating DFT-level descriptors, we also calculated descriptors at lower levels of theory using xTB, RDKit, and cclib version 1.7.2.^{50,51} These descriptors were used to train a separate model than DFT-level descriptors to reduce the computational cost of future predictions. Creating a model with these low-level descriptors removes the need for DFT calculations when predicting NCB stability.

These descriptors were calculated using the CSEARCH and QDESCP modules of AQME.³ Conformational sampling was not done using the already-established conformational sampling protocol since the calculations can become costly with the use of CREST and CENSO. The CSEARCH module of AQME was implemented using RDKit, and the QDESCP module utilized xTB to generate descriptors for each reduced NCB. In addition to the default keywords, we also used `--qdescp_atoms ['C1=C[N]C=CC1']` to calculate atomic descriptors at the N1 position of the 1,4-dihydropyridine ring. Atomic descriptors calculated at C were discarded since there were multiple present and it the physical meaning of these descriptors was unclear.

When all descriptors were calculated, we filtered them to ensure that all descriptors were meaningful. We removed categorical descriptors, such as those which count the number of instances of functional groups and any van der Waals Surface Area (VSA) descriptors. VSA descriptors include only information about what type of atom is present, something which is reflected in other descriptors already.

There were 63 descriptors which were given as input to the predictive model. Gasteiger partial charges⁵² from RDKit, as well as Mulliken⁵³ and CM5⁵⁴ partial charges on the N1 atom of the 1,4-dihydropyridinium ring from xTB were included. Also calculated were the nucleophilic ($f(+)$), electrophilic ($f(-)$), and radical ($f(rad)$) Fukui indices at the N1 atom of the NCBs.⁴⁹ The coordination number for the N1 atom were also calculated, representing how many bonds there

are to nitrogen in the ring. The dispersion coefficient C6 was also calculated at the N1 position of each NCB, as was the polarizability α . The polarizability α of an atom is the tendency of an atom to acquire a dipole in an electric field.⁵⁵ Also calculated in this workflow is the fractional occupation density (FOD)⁵⁶ on the N1 atom. FOD is given by:

$$\rho^{FOD}(r) = \sum_i^N (\delta_1 - \delta_2 f_i) |\varphi_i(r)|^2$$

where φ_i are molecular spin orbitals, f_i are the fractional orbital occupation numbers ($0 \leq f_i \leq 1$), δ_1 and δ_2 are constants, and the sum is taken over all electronic single-particle levels in the system.

⁵⁷ The FOD of an atom represents the static electron correlation that is localized on an atom. The values are also broken down into the s and p orbital proportions, or how the FOD is distributed among these orbital types. Also calculated for the s, p, and d orbitals on this atom are the proportions of electron population partitioned to each of these orbital types.

Molecular descriptors were also calculated while gathering these semi-empirical descriptors. Similar to how partial charges were calculated for the N1 atom, there are also descriptors which encapsulate the charge descriptions of the full molecule. These include the total charge of the molecule, the minimum and maximum values of the partial charges for the molecule, and the minimum and maximum values for the absolute partial charge. The difference between the minimum/maximum partial charge and the minimum/maximum absolute partial charge is that the partial charge considers the sign of the charge while the absolute partial charges only account for magnitude of the charge. For example, a molecule the minimum partial charge -0.9 could also be the maximum absolute partial charge with a value of 0.9. The E-State Index of an atom represents the electrotopological state index for atoms in molecules, combining electronic character and topological environment of each atom.⁵⁸ The minimum/maximum E-State Index and the minimum/maximum absolute E-State Index of the molecule are included as descriptors. HOMO and LUMO represent the energies in eV for the HOMO and LUMO of the molecule, respectively. The HOMO-LUMO gap is also given. Additionally, the number of valence electrons of the molecule were included. The descriptor FractionCSP3 represents the fraction of the molecule made up by sp^3 carbon atoms. The molecular weight of the NCB, the molecular weight of only the heavy atoms, and the exact molecular weight (including isotope contributions) were calculated for each NCB. Also calculated was the dipole moment of the molecule in units of Debye. The Fermi level

is a descriptor representing the highest occupied energy level occupied at absolute zero and is given in eV.⁵⁹ The SPS term is a scoring system to tell how complex a molecule is, accounting for proportions of sp³ carbon atoms and stereogenic carbon atoms.⁶⁰ This value is normalized by the number of heavy atoms to help account for size as well. SPS is given by:

$$SPS = \sum (h * s * r * n^2)$$

where *h* is the atom's hybridization term, *s* is the stereoisomeric term, *r* is the non-aromatic ring term, and *n* is the number of heavy atoms. Kappa values give details about the shape of the molecule.⁶¹ These values are focused around 4 quantities, the number of atoms, the number of paths of length 1, the number of paths of length 2, and the number of paths of length 3. A path is how many atoms are bound without any substituents. For example, octane has a path of length 8 while 6-methylheptane has a path length of only 7. Kappa1 tells about the complexity of acyclic molecules, Kappa2 stores information about the spatial density of atoms in a molecule, and Kappa3 encodes information about the centrality of branching in a molecule. The Chi values are used to characterize different structural attributes of molecules and are a weighted count of a given type of subgraph, or molecular representation.⁶¹ Chi indices represent a summation of the whole graph and focus on simple subgraphs. The number of a Chi index represent different types of subgraph corresponding to the number of connecting bonds present. For example, Chi0 has no edges present in the subgraph, or represents only an atom. Chi1 represents one bond, Chi2 represents paths, where there are two bonds presents, Chi3 and Chi4 also represent paths, but can give more detail about the arrangement of these bonds since they focus on molecular graph paths of lengths 3 and 4, respectively. There are three types of Chi index associated with each Chi number given in RDKit. ChiN is the Chi index of length N which does not account for the number of valence electrons, only the number of neighbors. ChiNv is the Chi index of length N which does account for the number of valence electrons. Finally, ChiNn is the Chi index of length N which accounts for the number of valence electrons, but does not include a heavy atom correction. The Balaban J value is a topological index which works to translate the chemical constitution of a molecule into numerical values. This descriptor has low degeneracy, meaning that multiple different isomers can give the same value, and increases with the number of rings present in a molecule. The Balaban J value is given by:

$$J = \frac{q}{\mu + 1} \sum_{edges\ i,j} (s_i s_j)^{-1/2}$$

where q is the number of edges in the molecular graph, s_i and s_j are given by the sums over rows or columns of the topological distance matrix of the molecule, respectively, and μ is given by:

$$\mu = q - n - x$$

where n is the number of atoms in the molecular graph and x is the cyclomatic number of the molecular graph.^{62,63} The Morgan fingerprint is a popular method of vectorizing molecular properties.⁶⁴ The number associated with this fingerprint is the radius considered. For example, the FpDensityMorgan1 descriptor represents the density of the Morgan fingerprint at only the starting atom. FpDensityMorgan2 represents the density of the Morgan fingerprint at the starting atom and any heavy atoms bound to your starting atom. FpDensityMorgan3 goes one bond further and represents anything within 2 bonds of the starting atom. The density of a Morgan fingerprint represents the number of unique atomic environments in the molecule within the radius specified. The IPC index of a molecule gives details on the structural complexity of the molecule, represented by the information content of the coefficients of the characteristic polynomial of the molecule's adjacency matrix.⁶⁵ The AvgIpc descriptor gives the IPC index divided by the total population, normalizing for molecular weight. The BertzCT descriptor is a topological descriptor of the molecule also meant to quantify the complexity of the molecule.⁶⁶ This descriptor is a sum of the complexity of bonds and the complexity of the heteroatoms in the molecule. The Hall-Kier α of a molecule is used to modify the atom count in a molecule.⁶¹ Because it is likely that non-sp³ carbon atoms make more or less of an impact on the shape of a molecule than sp³ carbons, this descriptor is meant to adjust the atom count to reflect these differences, given by:

$$\alpha = \left(r / r_{Csp^3} \right) - 1$$

where r is the covalent radius of the atom and r_{Csp^3} is the covalent radius of an sp³ carbon atom. Labute's approximate surface area (ASA) is the surface area of an atom not included in any other atoms by Van der Waal radii.⁶⁷ The MolMR descriptor is a measure of the molar refractivity of a molecule, or the total polarizability of a mole of the molecule.⁶⁸ This value is dependent on the temperature, index of refraction, and pressure of the system. MolLogP is the LogP value, or the octanol-water partition coefficient, of a molecule used as a measure of lipophilicity.⁶⁸ Both MolMR and MolLogP are calculated from SMARTS representations of the molecules. TPSA stands for the topological polar surface area of a molecule and is calculated by the sum of surface

areas of polar fragments in the molecule.⁶⁹ Finally, the QED value of a molecule is a quantitative estimate of druglikeness, calculated by:

$$QED = \left(\frac{1}{n} * \sum_{i=1}^n \ln(d_i) \right)$$

where n is the number of desirability functions d represented by molecular descriptors.⁷⁰

7 Predictive Modeling of NCB Stability with ROBERT

Predictive modeling of the stability of NCBs was done using ROBERT version 1.0.6.⁷¹ Starting with the DFT-level descriptors, different model architectures were used to train a series of predictive models and find the one with the highest performance (Figure S7). In partitioning the data, 10% of the data became the test set, while the remaining 90% of the data were partitioned into training and validation sets. All splits were done randomly. The different models included train:validation proportions of 60:40, 65:35, 70:30, 75:25, 80:20, 85:15, and 90:10 for the 90% of data points which were not included in the test set. There were also 4 different kinds of regression models considered: multivariate linear (MLR), neural network (NN), gradient-boosted (GB), and random forest (RF). A total of 28 models were trained to determine which combination gives the best model. Aside from selecting a larger range of train:validation:test splits to be used, ROBERT was run with all default settings. The final model architecture was selected based on the lowest RMSE values from the full array of models trained at the DFT-level after default permutation feature importance (PFI) analysis. The best model was an MLR model with a 101:18:13 train:validation:test split. This architecture was also used for the semi-empirical model to ensure proper comparisons between the two models.

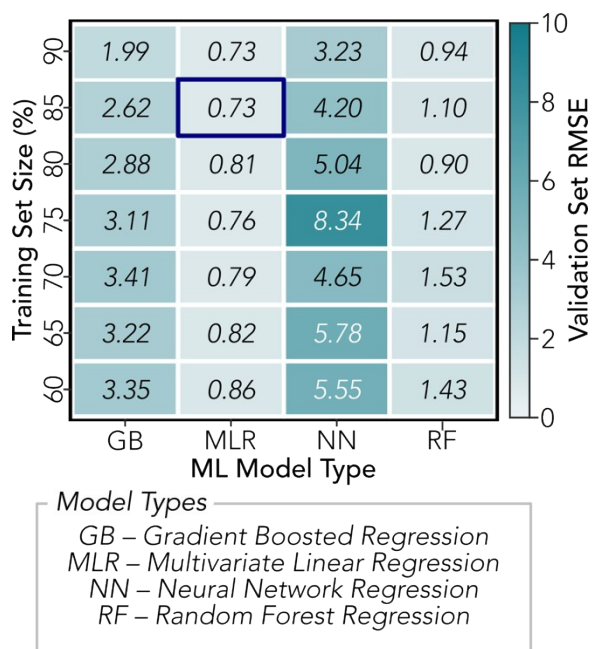


Figure S7. Heatmap showing the performance of varying model architectures following default permutation feature importance analysis in ROBERT. The highest-performing model is shown in the blue box.

Among all models tested, the MLR models out-performed other model types. This can, in part, be explained by the relatively low number of data points used in the training of these models. Large model types, such as neural networks, tend to be data hungry and require a large number of events per variable to perform well.⁷² Because our NCB library has only 132 total cofactors, or events, it was unlikely that a large neural network model would perform well. Gradient boosted regressors tend to be better than neural networks when dealing with small datasets, but they are not without issues. With small quantities of training data, the loss gradient used in making the next decision tree relies more on each individual datapoint, making this type of model more sensitive to outliers than other methods, such as random forest regression models. These qualities of gradient boosted regressors may explain the higher RMSE values compared to those of random forest or MLR models.⁷³ Better performance of MLR models compared to random forest regressors likely stems from the linear correlation between many of the descriptors and the predicted stability values. For the features selected as most important for the final model, many demonstrate a linear correlation with NCB stability (Figure S8). The shape of these distributions suggests that a linear regression

model would be most appropriate for this data, likely leading to the reduced RMSE values compared to random forest models.

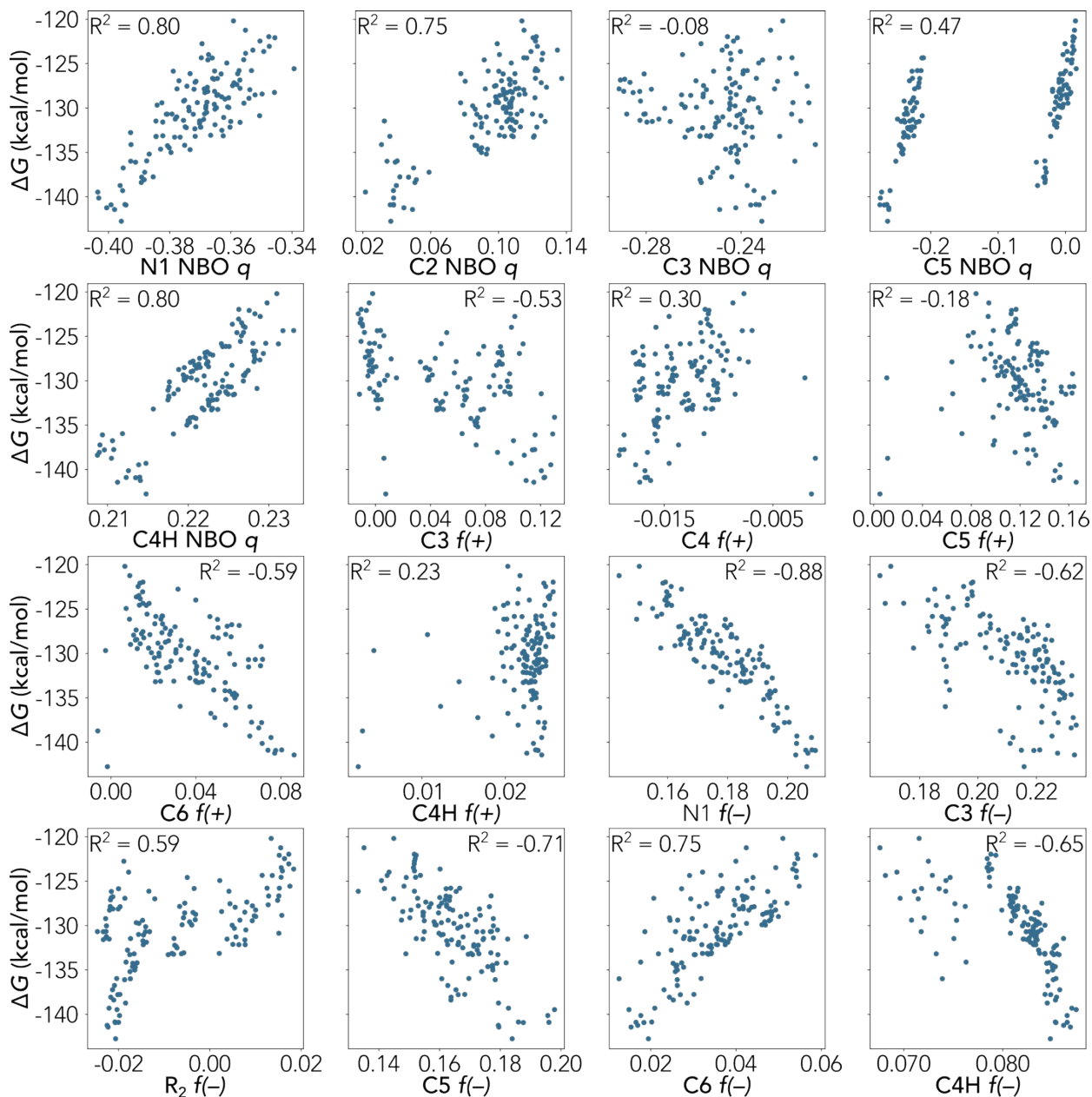


Figure S8. Univariate relationships between descriptors used to select model architecture and NCB stability. R^2 values are calculated using `r2_score` from SciKit Learn.⁷⁴

To ensure that our model was robust and generalizable, we conducted further model evaluation using the VERIFY module within ROBERT software (Table S4). This testing includes 5-fold cross-validation, y-mean, y-shuffle, and one-hot encoding tests and compares model performance

to the original validation RMSE with a 25% buffer. In this case, the RMSE of the validation set was 0.76, so 0.96 was the RMSE threshold used to determine if a test passed or failed. The 5-fold cross-validation splits the data into 5 groups, then uses 4 as the training set and 1 as the test set. This process is then repeated until all groups have been used as both training and testing data. This test is passed if the new RMSE is lower than the threshold, representing that the original model had an appropriate train:validation:test split. The y-mean test looks at the error of our model if all predicted values were equal to the mean y-value and is passed if the RMSE is higher than the threshold, showing that the model can predict values far from the mean y-value. The y-shuffle test shuffles the y-values so they are no longer associated with the original x-values and tests model performance. This test is passed if the RMSE is higher than the threshold, showing that the x-values are meaningful in making predictions in the model. Finally, the one-hot encoding test replaces x-values with 1 or 0 to test if the values of descriptors used in the model are meaningful, or if categorization is as effective. This test is passed if the RMSE is higher than the threshold, since the model performed better with the true x-values than with categorical assignments.

Table S4. VERIFY testing results from ROBERT to evaluate model generalizability.

<i>VERIFY Test</i>	<i>RMSE</i>	<i>Pass/Fail</i>
5-Fold Cross-Validation	0.89	Pass
Y-Mean	3.7	Pass
Y-Shuffle	6.0	Pass
One-Hot Encoding	3.7	Pass

Furthermore, to ensure an appropriate train:validation:test split for this data, we have visualized the data using principal component analysis, coloring points by which set they belong to (Figure S9). This analysis shows that the validation and test sets are well distributed among the chemical space of our NCB library, supporting the results from the 5-fold cross-validation that our data splits are appropriate in our predictive model.

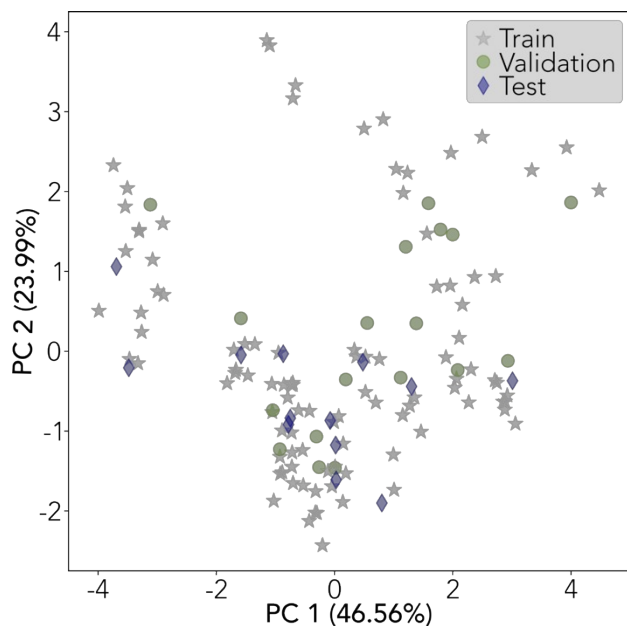


Figure S9. Principal component analysis (PCA) showing the NCB scope of this study with structures colored by which set (train:validation:test) they belong to for model training. The training set is shown in grey stars, the validation set in green circles, and the test set in blue diamonds.

In addition to training a model with DFT-level descriptors, we also trained a model using computationally cheaper semi-empirical descriptors (Figure S10). This allows predictions to be made faster than DFT allows and starts with only a SMILES representation as input. The stability metric, ΔG , used to train this model was still obtained from our DFT study to ensure accurate predictions. We used ROBERT software to train a second model to predict NCB stability, this time using the semi-empirical descriptors.⁷¹ To ensure our ability to compare the two models, we only trained the lower-level model using the same model architecture as was found to perform best for the DFT-level model, a MLR model with a 101:18:13 train:validation:test split.

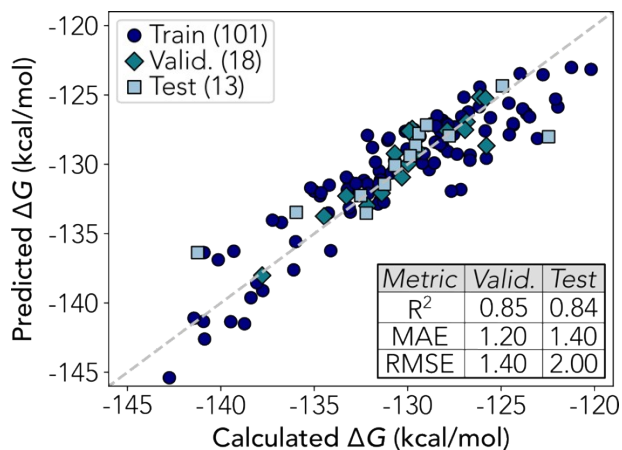


Figure S10. Parity plot and results for the best-performing predictive model trained with semi-empirical descriptors, a MLR with a 101:18:13 train:validation:test split using the 12 most important descriptors. Model performance metrics are shown at the bottom right of the graph for the validation and test sets.

The model trained with semi-empirical descriptors was also a high-performing model. While the MAE and RMSE were higher than those of the DFT-level model, these values are still within accepted computational accuracy, thus suggesting a strong predictive model. The quality of this model was assessed on the same metrics as the DFT-level model, those which ROBERT automatically performs. Details on these tests can be found in the documentation for ROBERT. Overall, the model results of the semi-empirical model were lower compared to the model trained with DFT-level descriptors, but it is encouraging that we were able to train such a high-quality model using descriptors that are much faster/cheaper to calculate. Lower accuracy is to be expected when using only semi-empirical descriptors, but the MAE and RMSE still being within typical DFT accuracy means that stability predictions can be more easily obtained in the future. It is also worth noting that this was only performed using the same model architecture as performed best

for the DFT-level model; there may be another model type or train:validation:test split that would yield even more accurate predictions.

To train the final models, we used a variation of the default PFI implemented in ROBERT. After descriptors were filtered with default settings by the CURATE module of ROBERT, we further examined the PFI scores assigned to each descriptor (Table S5), then trained models using 12 or less of the most important descriptors to maintain a 10:1 training data point to descriptor ratio. The final number of descriptors to use for the DFT-level model was determined based on model performance metrics (Table S6). This analysis led us to use the 8 most important descriptors, as any fewer descriptors results in substantial loss of accuracy for the model.

Table S5. PFI Scores and Errors for DFT-level and semi-empirical descriptors.

<i>DFT-Level Model</i>		<i>Semi-Empirical Model</i>	
<i>Descriptor</i>	<i>PFI Score</i>	<i>Descriptor</i>	<i>PFI Score</i>
C4H <i>f</i> (-)	2.421 ± 0.807	Number of valence electrons	8.858 ± 0.797
C3 <i>f</i> (-)	1.109 ± 0.185	Kappa1	8.416 ± 1.841
R ₂ <i>f</i> (-)	1.104 ± 0.337	LUMO	4.643 ± 0.473
C2 NBO partial charge	0.720 ± 0.139	SPS	4.582 ± 0.823
C3 NBO partial charge	0.456 ± 0.043	Minimum E-State Index	4.541 ± 1.080
C5 NBO partial charge	0.454 ± 0.113	Chi4n	2.387 ± 0.420
N1 NBO partial charge	0.428 ± 0.065	Balaban J	1.568 ± 0.454
C4H NBO partial charge	0.319 ± 0.030	Dipole moment	1.360 ± 0.277
C4 <i>f</i> (+)	0.288 ± 0.055	Kappa3	0.950 ± 0.219
N1 <i>f</i> (-)	0.208 ± 0.028	HOMO-LUMO gap	0.843 ± 0.290
C6 <i>f</i> (+)	0.202 ± 0.052	Dispersion coefficient C6 of the N1 atom	0.513 ± 0.203
C3 <i>f</i> (+)	0.153 ± 0.051	Fraction of sp ³ carbon atoms	0.409 ± 0.038
C6 <i>f</i> (-)	0.133 ± 0.031	Maximum absolute E-State Index	0.389 ± 0.140
C5 <i>f</i> (-)	0.105 ± 0.010	TPSA	0.241 ± 0.038

C4H $f(+)$	0.064 ± 0.012	N1 $f(-)$	0.200 ± 0.050
C5 $f(+)$	0.053 ± 0.011	MolLogP	0.080 ± 0.024
R ₂ NBO partial charge	0.029 ± 0.006	Partial charge on N1 atom	0.078 ± 0.077
C2 $f(-)$	0.028 ± 0.011	N_FOD p proportion	0.045 ± 0.031
R ₁ NBO partial charge	0.026 ± 0.013	Minimum absolute E-State Index	0.026 ± 0.013
R ₁ $f(-)$	0.026 ± 0.011	Minimum Partial Charge	0.012 ± 0.005
N1 $f(+)$	0.014 ± 0.006	Morgan Fingerprint Density 1	0.008 ± 0.016
C6 NBO partial charge	0.012 ± 0.006	Maximum Partial Charge	0.003 ± 0.008
LUMO molecular orbital value	0.003 ± 0.003	FOD s proportion of the N1 atom	0.000 ± 0.000
R ₁ $f(+)$	0.002 ± 0.003	---	---
C4 $f(-)$	0.002 ± 0.002	---	---
C2 $f(+)$	0.001 ± 0.002	---	---
C4 NBO partial charge	-0.001 ± 0.002	---	---

Table S6. Model performance metrics for DFT-level models varying number of descriptors.

<i>Metric</i>	<i>N=16</i> <i>(default)</i>	<i>N=12</i>	<i>N=10</i>	<i>N=8</i>	<i>N=6</i>	<i>N=5</i>	<i>N=4</i>
Test R ²	0.97	0.97	0.97	0.98	0.91	0.78	0.77
Test MAE	0.68	0.67	0.70	0.61	1.20	1.70	1.80
Test RMSE	0.81	0.79	0.81	0.70	1.40	2.10	2.20
Valid. R ²	0.96	0.96	0.96	0.96	0.95	0.89	0.75
Valid. MAE	0.59	0.58	0.80	0.50	0.79	1.30	1.60
Valid. RMSE	0.73	0.77	0.70	0.76	1.10	1.80	1.90

We then trained another MLR model with a 101:18:13 train:validation:test split using only semi-empirical descriptors, as mentioned above. We used the same procedure for selecting the final descriptors in this model as for the DFT-level model, which led us to selecting the 12 most

important descriptors (Table S7). Any fewer than 12 descriptors showed a drop in model performance. The final equations for the MLR models are shown in Table S8 and S9.

Table S7. Model performance metrics for semi-empirical models varying number of descriptors.

<i>Metric</i>	<i>N=17 (default)</i>	<i>N=12</i>	<i>N=10</i>	<i>N=8</i>	<i>N=6</i>	<i>N=5</i>	<i>N=4</i>
Test R ²	0.88	0.84	0.72	0.69	0.78	0.65	0.59
Test MAE	1.40	1.40	1.80	1.80	1.90	2.40	2.50
Test RMSE	1.70	2.00	2.40	2.60	2.40	3.00	3.10
Valid. R ²	0.87	0.85	0.83	0.85	0.83	0.53	0.52
Valid. MAE	1.10	1.20	1.30	1.10	1.10	2.10	1.90
Valid. RMSE	1.40	1.40	1.50	1.30	1.30	2.40	2.30

Table S8. Descriptors and associated (standardized) coefficients for the final DFT and semi-empirical MLR models.

<i>DFT</i>		<i>Semi-Empirical</i>	
<i>Descriptor</i>	<i>Coefficient</i>	<i>Descriptor</i>	<i>Coefficient</i>
Constant	-130.43	Constant	-130.58
C4H NBO Partial Charge	2.70	NumValenceElectrons	-8.91
C5 NBO Partial Charge	2.24	Kappa1	5.93
C3 <i>f</i> (-)	-1.60	LUMO (eV)	-5.62
C2 NBO Partial Charge	1.44	Chi4n	3.26
R ₂ <i>f</i> (-)	-0.98	Kappa3	3.14
C4H <i>f</i> (-)	0.73	BalabanJ	2.36
N1 NBO Partial Charge	0.67	FractionCSP3	-2.19
C3 NBO Partial Charge	0.37	Dipole Module (Debye)	1.86
--	--	N1 Dispersion Coefficient C6	-1.65
--	--	SPS	1.53
--	--	HOMO-LUMO gap (eV)	1.33
--	--	MinEStateIndex	-1.24

Table S9. Descriptors and associated (unstandardized) coefficients for the final DFT and semi-empirical MLR models.

<i>DFT</i>		<i>Semi-Empirical</i>	
<i>Descriptor</i>	<i>Coefficient</i>	<i>Descriptor</i>	<i>Coefficient</i>
C4H NBO Partial Charge	479.90	Constant	-168.27
Constant	-209.86	Chi4n	15.01
C4H <i>f</i> (-)	157.92	FractionCSP3	-13.10
C3 <i>f</i> (-)	-97.69	Kappa1	7.62
R ₂ <i>f</i> (-)	-70.25	BalabanJ	4.96
C2 NBO Partial Charge	51.72	LUMO (eV)	-3.30
N1 NBO Partial Charge	47.13	Kappa3	2.91
C3 NBO Partial Charge	19.71	MinEStateIndex	-2.45
C5 NBO Partial Charge	19.34	HOMO-LUMO gap (eV)	1.76
--	--	NumValenceElectrons	-0.57
--	--	N1 Dispersion Coefficient C6	-0.56
--	--	SPS	0.27
--	--	Dipole Module (Debye)	0.27

Another metric that we used to test the accuracy of our models was the Spearman correlation (Table S10).⁷⁵ This statistical test gives information into the rank-ordering of datapoints. Because we do not need information about the actual value of ΔG from these models, but rather stability relative to other structures, the Spearman correlation is a key test to ensure model success. The high correlation values and low p-values from the comparisons with our DFT-calculated stabilities show that both models do well in determining the correct ranking of the stabilities of our NCB library and are therefore good models for this purpose.

Table S10. Spearman correlation results comparing our DFT-calculated stability values with model predictions.

<i>Model</i>	<i>Spearman Correlation</i>	<i>T-Test p-Value</i>
DFT	0.974	1.80e-85

Semi-Empirical	0.915	5.80e-53
----------------	-------	----------

8 Mean Stabilities of Each Substituent

After models were trained, we also examined the trends that we saw in the descriptors and models. Based on the different relationships present with different substituents in Figure 7 (main text), we decided to find the mean stability of each substituent in our library (Table S11). These data show that **E** is the most stable R_1 substituent (followed by **F**), **4** is the most stable substituent at the R_2 position, and **b** is the most stable R_3 substituent. We used these analyses to aid in the design of stable, out-of-sample NCBs.

Table S11. Mean stability of each substituent at R_1 , R_2 , and R_3 positions.

R_1 Substituent		R_2 Substituent		R_3 Substituent	
<i>ID</i>	<i>Stability</i>	<i>ID</i>	<i>Stability</i>	<i>ID</i>	<i>Stability</i>
A	-131.6 ± 4.2	1	-131.8 ± 2.5	a	-132.2 ± 4.3
B	-131.9 ± 4.4	2	-128.3 ± 2.4	b	-128.7 ± 4.4
C	-130.3 ± 4.6	3	-129.4 ± 2.1	--	--
D	-131.7 ± 4.7	4	-125.1 ± 2.9	--	--
E	-126.6 ± 3.6	5	-138.1 ± 2.8	--	--
F	-130.0 ± 4.5	6	-130.2 ± 2.5	--	--
G	-131.1 ± 4.4	--	--	--	--
H	-131.3 ± 4.6	--	--	--	--
I	-131.4 ± 4.7	--	--	--	--
J	-127.8 ± 3.9	--	--	--	--
K	-131.6 ± 4.8	--	--	--	--

9 Generation and Testing of Out-of-Sample NCBs

The descriptors used to train the final DFT-level predictive model were further analyzed for trends in the data. The DFT-level model descriptors were used rather than the semi-empirical descriptors due to stronger model performance. Inspecting the correlation between each descriptor and the

stability metric, we were able to determine that some substituents stood out as more stable than the rest at each position. Methyl R_3 substituents are more stable than their hydrogen counterparts, aldehydes as the R_2 substituents show high stability, and aryl R_1 substituents tend to show the highest stability on average (Figure 6 in the main text). Using these trends, we proposed new substituents at each position and analyzed each new structure. Stabilities for these novel NCBs were calculated using the same procedure as those in our library. We found that these novel structures were among the most stable in our library, with some showing higher stability than any structures already in the library (Figure S11).

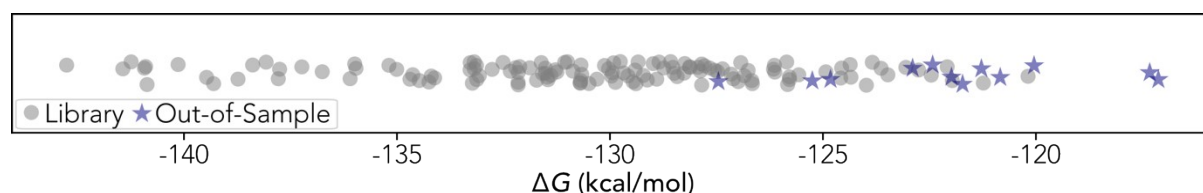


Figure S11. Representation of NCB stabilities from this study. Grey circles represent structures which were in our original library, blue stars represent the novel NCBs designed for improved stability.

We also modeled TS A-I for each novel structure to verify the higher stabilities demonstrated in our designed NCBs. Examining the correlation between ΔG and ΔG^\ddagger for the new cofactor structures in conjunction with the existing structures still shows a high correlation, evidenced by an R^2 value of 0.91 (Figure S12, Table S12).

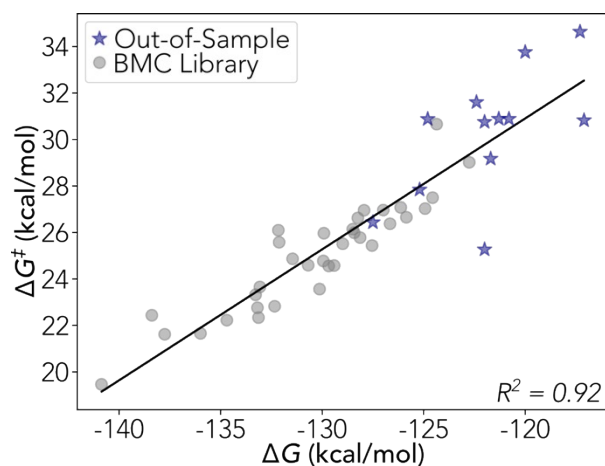


Figure S12. Correlation between ΔG and ΔG^\ddagger for the first step of NCB degradation. Values for ΔG were obtained with PBE0-D3(BJ)/def2-TZVP/SMD(water)//PBE0-D3(BJ)/6-31+G(d)/SMD(water).^{6-15,19-28} Values for ΔG^\ddagger were computed with ω B97M-V/def2-TZVP/SMD(water)//PBE0-D3(BJ)/6-31+G(d)/SMD(water).^{6-15,19-29} Structures from our original library are shown as grey circles while our new NCBs are shown as blue stars.

Table S12. Values of ΔG and ΔG^\ddagger for the new NCBs designed in this work. ΔG values are at PBE0-D3(BJ)/def2-TZVP/SMD(water)//PBE0-D3(BJ)/6-31+G(d)/SMD(water). ΔG^\ddagger values are at ω B97M-V/def2-TZVP/SMD(water)//PBE0-D3(BJ)/6-31+G(d)/SMD(water).

<i>NCB</i>	ΔG (kcal/mol)	ΔG^\ddagger (kcal/mol)
R_{1sub-I}	-122.0	30.8
R_{1sub-II}	-120.8	30.9
R_{1sub-III}	-121.3	30.9
R_{1sub-IV}	-117.3	34.6
R_{1sub-V}	-122.4	31.6
R_{1sub-VI}	-121.7	29.2
R_{2sub-I}	-124.8	30.9
R_{2sub-II}	-125.2	27.8
R_{2sub-III}	-127.5	26.4
R_{2sub-IV}	-120.0	33.8
R_{3sub-I}	-122.9	25.3
R_{3sub-II}	-117.1	30.8

Finally, we gathered DFT and semi-empirical descriptors for these novel NCBs using the same procedure as we did for structures in our library. This allowed us to test our models' performance against out-of-sample structures to ensure that our models are generalizable within NCBs. This was done by implementing only the PREDICT module of ROBERT, allowing us to make predictions without retraining the model, and we obtained stability predictions for all novel NCBs (Table S13). The semi-empirical model had more low-accuracy predictions than the DFT model.

Of the 6 structures which had low-accuracy predictions, 5 of them had descriptor values outside the range seen in the full library for at least one of the 5 most important descriptors. This is likely what led to the poor predictions for these structures, explained by differences in the general structure and properties from molecules in the original library and the model's lack of ability to extrapolate.

Table S13. Novel NCB stabilities and predicted stabilities with values in kcal/mol.

<i>Cofactor</i>	<i>Calculated Stability</i>	<i>DFT Predicted Stability</i>	<i>Prediction Error</i>	<i>Semi-Empirical Predicted Stability</i>	<i>Prediction Error</i>
R₁sub-I	-122.0	-120.9	1.1	-128.3	-6.3
R₁sub-II	-120.8	-120.3	0.5	-122.8	-2.0
R₁sub-III	-121.3	-120.5	0.8	-120.6	0.7
R₁sub-IV	-117.3	-114.9	2.4	-115.4	1.9
R₁sub-V	-122.4	-121.2	1.2	-125.1	-2.7
R₁sub-VI	-121.7	-120.6	1.1	-88.7	33.0
R₂sub-I	-124.8	-111.0	13.8	-125.2	-0.4
R₂sub-II	-125.2	-117.2	8.0	-122.7	2.5
R₂sub-III	-127.5	-126.6	0.9	-115.7	11.8
R₂sub-IV	-120.0	-109.9	10.1	-118.5	1.5
R₃sub-I	-122.9	-122.3	0.6	-108.4	14.5
R₃sub-II	-117.1	-120.0	-2.9	-104.0	13.1

In an effort to ensure that these predictions are within the scope of our model, we visualized the out-of-sample NCB structures in the chemical space of the library (Figure S13). Showing the new out-of-sample NCBs in chemical space relative to our existing library, the structures fall within the chemical space we would expect our model to predict. It is important to note that should future studies design new NCBs and wish to predict stability, it is important to consider whether the new NCB structures fall within the chemical space of our library which our model is trained on.

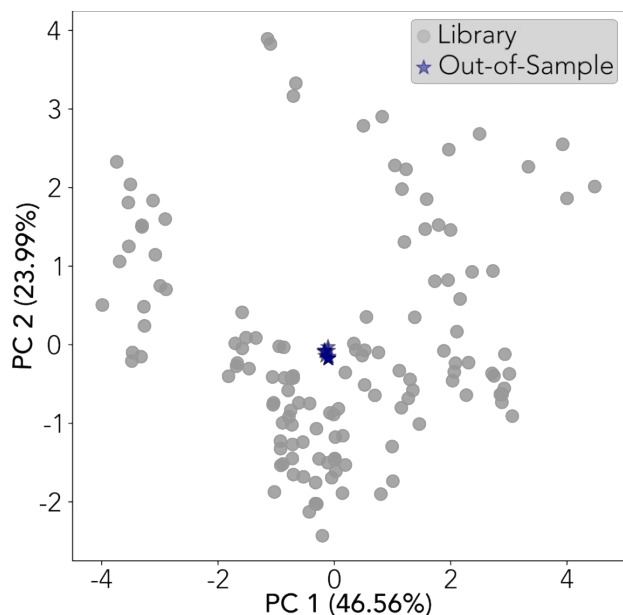


Figure S13. Principal component analysis (PCA) showing the full NCB scope of this study. Grey circles represent structures which were in our expanded library of 132 NCBs and blue stars represent the new out-of-sample NCBs designed following predictive modeling. The PCs were calculated only from our library to match the other representations of the data.

References

- (1) Rdkit/Rdkit: 2022_03_1b1 (Q1 2022) Release. <https://doi.org/10.5281/zenodo.6367148>.
- (2) O'Boyle, N. M.; Banck, M.; James, C. A.; Morley, C.; Vandermeersch, T.; Hutchison, G. R. Open Babel: An Open Chemical Toolbox. *J. Cheminformatics* **2011**, *3* (1), 33. <https://doi.org/10.1186/1758-2946-3-33>.
- (3) Alegre-Requena, J. V.; Sowndarya S. V., S.; Pérez-Soto, R.; Alturaifi, T. M.; Paton, R. S. AQME: Automated Quantum Mechanical Environments for Researchers and Educators. *WIREs Comput. Mol. Sci.* **2023**, *13* (5), e1663. <https://doi.org/10.1002/wcms.1663>.
- (4) Nowak, C.; Pick, A.; Csepei, L.-I.; Sieber, V. Characterization of Biomimetic Cofactors According to Stability, Redox Potentials, and Enzymatic Conversion by NADH Oxidase from *Lactobacillus Pentosus*. *ChemBioChem* **2017**, *18* (19), 1944–1949. <https://doi.org/10.1002/cbic.201700258>.
- (5) Alivisatos, S. G. A.; Ungar, F.; Abraham, G. Non-Enzymatic Interactions of Reduced Coenzyme I with Inorganic Phosphate and Certain Other Anions. *Nature* **1964**, *203* (4948), 973–975. <https://doi.org/10.1038/203973a0>.
- (6) Rassolov, V. A.; Pople, J. A.; Ratner, M. A.; Windus, T. L. 6-31G* Basis Set for Atoms K through Zn. *J. Chem. Phys.* **1998**, *109* (4), 1223–1229. <https://doi.org/10.1063/1.476673>.
- (7) Rassolov, V. A.; Ratner, M. A.; Pople, J. A.; Redfern, P. C.; Curtiss, L. A. 6-31G* Basis Set for Third-Row Atoms. *J. Comput. Chem.* **2001**, *22* (9), 976–984. <https://doi.org/10.1002/jcc.1058>.

- (8) Hariharan, P. C.; Pople, J. A. Accuracy of AH n Equilibrium Geometries by Single Determinant Molecular Orbital Theory. *Mol. Phys.* **1974**, *27* (1), 209–214. <https://doi.org/10.1080/00268977400100171>.
- (9) Binning Jr., R. C.; Curtiss, L. A. Compact Contracted Basis Sets for Third-Row Atoms: Ga–Kr. *J. Comput. Chem.* **1990**, *11* (10), 1206–1216. <https://doi.org/10.1002/jcc.540111013>.
- (10) Blaudeau, J.-P.; McGrath, M. P.; Curtiss, L. A.; Radom, L. Extension of Gaussian-2 (G2) Theory to Molecules Containing Third-Row Atoms K and Ca. *J. Chem. Phys.* **1997**, *107* (13), 5016–5021. <https://doi.org/10.1063/1.474865>.
- (11) Francl, M. M.; Pietro, W. J.; Hehre, W. J.; Binkley, J. S.; Gordon, M. S.; DeFrees, D. J.; Pople, J. A. Self-consistent Molecular Orbital Methods. XXIII. A Polarization-type Basis Set for Second-row Elements. *J. Chem. Phys.* **1982**, *77* (7), 3654–3665. <https://doi.org/10.1063/1.444267>.
- (12) Ditchfield, R.; Hehre, W. J.; Pople, J. A. Self-Consistent Molecular-Orbital Methods. IX. An Extended Gaussian-Type Basis for Molecular-Orbital Studies of Organic Molecules. *J. Chem. Phys.* **1971**, *54* (2), 724–728. <https://doi.org/10.1063/1.1674902>.
- (13) Hehre, W. J.; Ditchfield, R.; Pople, J. A. Self—Consistent Molecular Orbital Methods. XII. Further Extensions of Gaussian—Type Basis Sets for Use in Molecular Orbital Studies of Organic Molecules. *J. Chem. Phys.* **1972**, *56* (5), 2257–2261. <https://doi.org/10.1063/1.1677527>.
- (14) Hariharan, P. C.; Pople, J. A. The Influence of Polarization Functions on Molecular Orbital Hydrogenation Energies. *Theor. Chim. Acta* **1973**, *28* (3), 213–222. <https://doi.org/10.1007/BF00533485>.
- (15) Gordon, M. S. The Isomers of Silacyclopropane. *Chem. Phys. Lett.* **1980**, No. 76, 163–168. [https://doi.org/10.1016/0009-2614\(80\)80628-2](https://doi.org/10.1016/0009-2614(80)80628-2).
- (16) Black, W. B.; Perea, S.; Li, H. Design, Construction, and Application of Noncanonical Redox Cofactor Infrastructures. *Curr. Opin. Biotechnol.* **2023**, *84*, 103019. <https://doi.org/10.1016/j.copbio.2023.103019>.
- (17) Zachos, I.; Güner, S.; Essert, A.; Lommes, P.; Sieber, V. Boosting Artificial Nicotinamide Cofactor Systems. *Chem. Commun.* **2022**, *58* (85), 11945–11948. <https://doi.org/10.1039/D2CC03423A>.
- (18) Nowak, C.; Pick, A.; Lommes, P.; Sieber, V. Enzymatic Reduction of Nicotinamide Biomimetic Cofactors Using an Engineered Glucose Dehydrogenase: Providing a Regeneration System for Artificial Cofactors. *ACS Catal.* **2017**, *7* (8), 5202–5208. <https://doi.org/10.1021/acscatal.7b00721>.
- (19) Grimme, S.; Ehrlich, S.; Goerigk, L. Effect of the Damping Function in Dispersion Corrected Density Functional Theory. *J. Comput. Chem.* **2011**, *32* (7), 1456–1465. <https://doi.org/10.1002/jcc.21759>.
- (20) Grimme, S.; Antony, J.; Ehrlich, S.; Krieg, H. A Consistent and Accurate Ab Initio Parametrization of Density Functional Dispersion Correction (DFT-D) for the 94 Elements H–Pu. *J. Chem. Phys.* **2010**, *132* (15), 154104. <https://doi.org/10.1063/1.3382344>.
- (21) Weigend, F. Accurate Coulomb-Fitting Basis Sets for H to Rn. *Phys. Chem. Chem. Phys.* **2006**, No. 6, 1057–1065.
- (22) Weigend, F.; Ahlrichs, R. Balanced Basis Sets of Split Valence, Triple Zeta Valence and Quadruple Zeta Valence Quality for H to Rn: Design and Assessment of Accuracy. *Phys. Chem. Chem. Phys.* **2005**, *7* (18), 3297–3305. <https://doi.org/10.1039/B508541A>.

- (23) Schäfer, A.; Horn, H.; Ahlrichs, R. Fully Optimized Contracted Gaussian Basis Sets for Atoms Li to Kr. *J. Chem. Phys.* **1992**, *97* (4), 2571–2577. <https://doi.org/10.1063/1.463096>.
- (24) Schäfer, A.; Huber, C.; Ahlrichs, R. Fully Optimized Contracted Gaussian Basis Sets of Triple Zeta Valence Quality for Atoms Li to Kr. *J. Chem. Phys.* **1994**, *100* (8), 5829–5835. <https://doi.org/10.1063/1.467146>.
- (25) Ernzerhof, M.; Scuseria, G. E. Assessment of the Perdew–Burke–Ernzerhof Exchange–Correlation Functional. *J. Chem. Phys.* **1999**, *110* (11), 5029–5036. <https://doi.org/10.1063/1.478401>.
- (26) Perdew, J. P.; Burke, K.; Ernzerhof, M. Generalized Gradient Approximation Made Simple. *Phys. Rev. Lett.* **1996**, *77* (18), 3865–3868. <https://doi.org/10.1103/PhysRevLett.77.3865>.
- (27) Adamo, C.; Barone, V. Toward Reliable Density Functional Methods without Adjustable Parameters: The PBE0 Model. *J. Chem. Phys.* **1999**, *110* (13), 6158–6170. <https://doi.org/10.1063/1.478522>.
- (28) Marenich, A. V.; Cramer, C. J.; Truhlar, D. G. Universal Solvation Model Based on Solute Electron Density and on a Continuum Model of the Solvent Defined by the Bulk Dielectric Constant and Atomic Surface Tensions. *J. Phys. Chem. B* **2009**, *113* (18), 6378–6396. <https://doi.org/10.1021/jp810292n>.
- (29) Mardirossian, N.; Head-Gordon, M. ω B97M-V: A Combinatorially Optimized, Range-Separated Hybrid, Meta-GGA Density Functional with VV10 Nonlocal Correlation. *J. Chem. Phys.* **2016**, *144* (21), 214110. <https://doi.org/10.1063/1.4952647>.
- (30) Pracht, P.; Bohle, F.; Grimme, S. Automated Exploration of the Low-Energy Chemical Space with Fast Quantum Chemical Methods. *Phys. Chem. Chem. Phys.* **2020**, *22* (14), 7169–7192. <https://doi.org/10.1039/C9CP06869D>.
- (31) Grimme, S. Exploration of Chemical Compound, Conformer, and Reaction Space with Meta-Dynamics Simulations Based on Tight-Binding Quantum Chemical Calculations. *J. Chem. Theory Comput.* **2019**, *15* (5), 2847–2862. <https://doi.org/10.1021/acs.jctc.9b00143>.
- (32) Spicher, S.; Grimme, S. Robust Atomistic Modeling of Materials, Organometallic, and Biochemical Systems. *Angew. Chem. Int. Ed.* **2020**, *59* (36), 15665–15673. <https://doi.org/10.1002/anie.202004239>.
- (33) Bannwarth, C.; Ehlert, S.; Grimme, S. GFN2-xTB—An Accurate and Broadly Parametrized Self-Consistent Tight-Binding Quantum Chemical Method with Multipole Electrostatics and Density-Dependent Dispersion Contributions. *J. Chem. Theory Comput.* **2019**, *15* (3), 1652–1671. <https://doi.org/10.1021/acs.jctc.8b01176>.
- (34) Bannwarth, C.; Caldeweyher, E.; Ehlert, S.; Hansen, A.; Pracht, P.; Seibert, J.; Spicher, S.; Grimme, S. Extended Tight-Binding Quantum Chemistry Methods. *WIREs Comput. Mol. Sci.* **2021**, *11* (2), e1493. <https://doi.org/10.1002/wcms.1493>.
- (35) Grimme, S.; Bohle, F.; Hansen, A.; Pracht, P.; Spicher, S.; Stahn, M. Efficient Quantum Chemical Calculation of Structure Ensembles and Free Energies for Nonrigid Molecules. *J. Phys. Chem. A* **2021**, *125* (19), 4039–4054. <https://doi.org/10.1021/acs.jpca.1c00971>.
- (36) Neese, F. Software Update: The ORCA Program System—Version 5.0. *WIREs Comput. Mol. Sci.* **2022**, *12* (5), e1606. <https://doi.org/10.1002/wcms.1606>.
- (37) Brandenburg, J. G.; Bannwarth, C.; Hansen, A.; Grimme, S. B97-3c: A Revised Low-Cost Variant of the B97-D Density Functional Method. *J. Chem. Phys.* **2018**, *148* (6), 064104. <https://doi.org/10.1063/1.5012601>.

- (38) Grimme, S.; Hansen, A.; Ehlert, S.; Mewes, J.-M. r2SCAN-3c: A “Swiss Army Knife” Composite Electronic-Structure Method. *J. Chem. Phys.* **2021**, *154* (6), 064103. <https://doi.org/10.1063/5.0040021>.
- (39) Frisch, M. J.; Trucks, G. W.; Schlegel, H. B.; Scuseria, G. E.; Robb, M. A.; Cheeseman, J. R.; Scalmani, G.; Barone, V.; Petersson, G. A.; Nakatsuji, H.; Li, X.; Caricato, M.; Marenich, A. V.; Bloino, J.; Janesko, B. G.; Gomperts, R.; Mennucci, B.; Hratchian, H. P.; Ortiz, J. V.; Izmaylov, A. F.; Sonnenberg, J. L.; Williams-Young, D.; Ding, F.; Lipparini, F.; Egidi, F.; Goings, J.; Peng, B.; Petrone, A.; Henderson, T.; Ranasinghe, D.; Zakrzewski, V. G.; Gao, J.; Rega, N.; Zheng, G.; Liang, W.; Hada, M.; Ehara, M.; Toyota, K.; Fukuda, R.; Hasegawa, J.; Ishida, M.; Nakajima, T.; Honda, Y.; Kitao, O.; Nakai, H.; Vreven, T.; Throssell, K.; Montgomery, J. A., Jr.; Peralta, J. E.; Ogliaro, F.; Bearpark, M. J.; Heyd, J. J.; Brothers, E. N.; Kudin, K. N.; Staroverov, V. N.; Keith, T. A.; Kobayashi, R.; Normand, J.; Raghavachari, K.; Rendell, A. P.; Burant, J. C.; Iyengar, S. S.; Tomasi, J.; Cossi, M.; Millam, J. M.; Klene, M.; Adamo, C.; Cammi, R.; Ochterski, J. W.; Martin, R. L.; Morokuma, K.; Farkas, O.; Foresman, J. B.; Fox, D. J. Gaussian 16, Revision C.01, 2016.
- (40) Zhao, Y.; Truhlar, D. G. The M06 Suite of Density Functionals for Main Group Thermochemistry, Thermochemical Kinetics, Noncovalent Interactions, Excited States, and Transition Elements: Two New Functionals and Systematic Testing of Four M06-Class Functionals and 12 Other Functionals. *Theor. Chem. Acc.* **2008**, *120* (1), 215–241. <https://doi.org/10.1007/s00214-007-0310-x>.
- (41) Zhao, Y.; Truhlar, D. G. Design of Density Functionals That Are Broadly Accurate for Thermochemistry, Thermochemical Kinetics, and Nonbonded Interactions. *J. Phys. Chem. A* **2005**, *109* (25), 5656–5667. <https://doi.org/10.1021/jp050536c>.
- (42) Marques, M. A. L.; Oliveira, M. J. T.; Burnus, T. Libxc: A Library of Exchange and Correlation Functionals for Density Functional Theory. *Comput. Phys. Commun.* **2012**, *183* (10), 2272–2281. <https://doi.org/10.1016/j.cpc.2012.05.007>.
- (43) Lehtola, S.; Steigemann, C.; Oliveira, M. J. T.; Marques, M. A. L. Recent Developments in Libxc — A Comprehensive Library of Functionals for Density Functional Theory. *SoftwareX* **2018**, *7*, 1–5. <https://doi.org/10.1016/j.softx.2017.11.002>.
- (44) Hujo, W.; Grimme, S. Performance of the van Der Waals Density Functional VV10 and (Hybrid)GGA Variants for Thermochemistry and Noncovalent Interactions. *J. Chem. Theory Comput.* **2011**, *7* (12), 3866–3871. <https://doi.org/10.1021/ct200644w>.
- (45) Valeev, E. F. Libint: A Library for the Evaluation of Molecular Integrals of Many-Body Operators over Gaussian Functions. <http://libint.valeyev.net/>.
- (46) Vydrov, O. A.; Van Voorhis, T. Nonlocal van Der Waals Density Functional: The Simpler the Better. *J. Chem. Phys.* **2010**, *133* (24), 244103. <https://doi.org/10.1063/1.3521275>.
- (47) Bogojeski, M.; Vogt-Maranto, L.; Tuckerman, M. E.; Müller, K.-R.; Burke, K. Quantum Chemical Accuracy from Density Functional Approximations via Machine Learning. *Nat. Commun.* **2020**, *11* (1), 5223. <https://doi.org/10.1038/s41467-020-19093-1>.
- (48) Glendening, E. D.; Landis, C. R.; Weinhold, F. NBO 7.0: New Vistas in Localized and Delocalized Chemical Bonding Theory. *J. Comput. Chem.* **2019**, *40* (25), 2234–2241. <https://doi.org/10.1002/jcc.25873>.
- (49) Yang, W.; Parr, R. G. Hardness, Softness, and the Fukui Function in the Electronic Theory of Metals and Catalysis. *Proc. Natl. Acad. Sci.* **1985**, *82* (20), 6723–6726. <https://doi.org/10.1073/pnas.82.20.6723>.

- (50) O'boyle, N. M.; Tenderholt, A. L.; Langner, K. M. Cclib: A Library for Package-Independent Computational Chemistry Algorithms. *J. Comput. Chem.* **2008**, *29* (5), 839–845. <https://doi.org/10.1002/jcc.20823>.
- (51) Release of Cclib Version 1.7. <https://doi.org/10.5281/zenodo.4420433>.
- (52) Gasteiger, J.; Marsili, M. Iterative Partial Equalization of Orbital Electronegativity—A Rapid Access to Atomic Charges. *Tetrahedron* **1980**, *36* (22), 3219–3228. [https://doi.org/10.1016/0040-4020\(80\)80168-2](https://doi.org/10.1016/0040-4020(80)80168-2).
- (53) Mulliken, R. S. Electronic Population Analysis on LCAO–MO Molecular Wave Functions. I. *J. Chem. Phys.* **1955**, *23* (10), 1833–1840. <https://doi.org/10.1063/1.1740588>.
- (54) Marenich, A. V.; Jerome, S. V.; Cramer, C. J.; Truhlar, D. G. Charge Model 5: An Extension of Hirshfeld Population Analysis for the Accurate Description of Molecular Interactions in Gaseous and Condensed Phases. *J. Chem. Theory Comput.* **2012**, *8* (2), 527–541. <https://doi.org/10.1021/ct200866d>.
- (55) Vishwakarma, G.; Sonpal, A.; Pradhan, A.; Haghghatlari, M.; Afzal, M. A. F.; Hachmann, J. Design of Organic Materials with Tailored Optical Properties: Predicting Quantum-Chemical Polarizabilities and Derived Quantities. In *Quantum Chemistry in the Age of Machine Learning*; 2022; pp 653–674.
- (56) Grimme, S.; Hansen, A. A Practicable Real-Space Measure and Visualization of Static Electron-Correlation Effects. *Angew. Chem. Int. Ed.* **2015**, *54* (42), 12308–12313. <https://doi.org/10.1002/anie.201501887>.
- (57) Grimme, S.; Hansen, A. A Practicable Real-Space Measure and Visualization of Static Electron-Correlation Effects. *Angew. Chem. Int. Ed.* **2015**, *54* (42), 12308–12313. <https://doi.org/10.1002/anie.201501887>.
- (58) Kier, L. B.; Hall, L. H. An Electrotopological-State Index for Atoms in Molecules. *Pharm. Res.* **1990**, *7* (8), 801–807. <https://doi.org/10.1023/A:1015952613760>.
- (59) Reiss, H. The Fermi Level and the Redox Potential. *J. Phys. Chem.* **1985**, *89* (18), 3783–3791. <https://doi.org/10.1021/j100264a005>.
- (60) Krzyzanowski, A.; Pahl, A.; Grigalunas, M.; Waldmann, H. Spacial Score—A Comprehensive Topological Indicator for Small-Molecule Complexity. *J. Med. Chem.* **2023**, *66* (18), 12739–12750. <https://doi.org/10.1021/acs.jmedchem.3c00689>.
- (61) Hall, L. H.; Kier, L. B. The Molecular Connectivity Chi Indexes and Kappa Shape Indexes in Structure-Property Modeling. In *Reviews in Computational Chemistry*; John Wiley & Sons, Ltd, 1991; pp 367–422. <https://doi.org/10.1002/9780470125793.ch9>.
- (62) Balaban, A. T. Topological Indices Based on Topological Distances in Molecular Graphs. *Pure Appl. Chem.* **1983**, *55* (2), 199–206. <https://doi.org/10.1351/pac198855020199>.
- (63) Balaban, A. T. Highly Discriminating Distance-Based Topological Index. *Chem. Phys. Lett.* **1982**, *89* (5), 399–404. [https://doi.org/10.1016/0009-2614\(82\)80009-2](https://doi.org/10.1016/0009-2614(82)80009-2).
- (64) Rogers, D.; Hahn, M. Extended-Connectivity Fingerprints. *J. Chem. Inf. Model.* **2010**, *50* (5), 742–754. <https://doi.org/10.1021/ci100050t>.
- (65) Nolte, T. M.; Peijnenburg, W. J. G. M.; Hendriks, A. Jan.; van de Meent, D. Quantitative Structure-Activity Relationships for Green Algae Growth Inhibition by Polymer Particles. *Chemosphere* **2017**, *179*, 49–56. <https://doi.org/10.1016/j.chemosphere.2017.03.067>.
- (66) Bertz, S. H. The First General Index of Molecular Complexity. *J. Am. Chem. Soc.* **1981**, *103* (12), 3599–3601. <https://doi.org/10.1021/ja00402a071>.
- (67) Labute, P. A Widely Applicable Set of Descriptors. *J. Mol. Graph. Model.* **2000**, *18* (4), 464–477. [https://doi.org/10.1016/S1093-3263\(00\)00068-1](https://doi.org/10.1016/S1093-3263(00)00068-1).

- (68) Wildman, S. A.; Crippen, G. M. Prediction of Physicochemical Parameters by Atomic Contributions. *J. Chem. Inf. Comput. Sci.* **1999**, *39* (5), 868–873. <https://doi.org/10.1021/ci9903071>.
- (69) Ertl, P.; Rohde, B.; Selzer, P. Fast Calculation of Molecular Polar Surface Area as a Sum of Fragment-Based Contributions and Its Application to the Prediction of Drug Transport Properties. *J. Med. Chem.* **2000**, *43* (20), 3714–3717. <https://doi.org/10.1021/jm000942e>.
- (70) Bickerton, G. R.; Paolini, G. V.; Besnard, J.; Muresan, S.; Hopkins, A. L. Quantifying the Chemical Beauty of Drugs. *Nat. Chem.* **2012**, *4* (2), 90–98. <https://doi.org/10.1038/nchem.1243>.
- (71) Dalmau, D.; Requena, J. V. A. ROBERT: Bridging the Gap between Machine Learning and Chemistry. ChemRxiv November 7, 2023. <https://doi.org/10.26434/chemrxiv-2023-k994h>.
- (72) van der Ploeg, T.; Austin, P. C.; Steyerberg, E. W. Modern Modelling Techniques Are Data Hungry: A Simulation Study for Predicting Dichotomous Endpoints. *BMC Med. Res. Methodol.* **2014**, *14* (1), 137. <https://doi.org/10.1186/1471-2288-14-137>.
- (73) Li, A. H.; Bradic, J. Boosting in the Presence of Outliers: Adaptive Classification With Nonconvex Loss Functions. *J. Am. Stat. Assoc.* **2018**, *113* (522), 660–674. <https://doi.org/10.1080/01621459.2016.1273116>.
- (74) Pedregosa, F.; Varoquaux, G.; Gramfort, A.; Michel, V.; Thirion, B.; Grisel, O.; Blondel, M.; Prettenhofer, P.; Weiss, R.; Dubourg, V.; Vanderplas, J.; Passos, A.; Cournapeau, D.; Brucher, M.; Perrot, M.; Duchesnay, É. Scikit-Learn: Machine Learning in Python. *J. Mach. Learn. Res.* **2011**, *12* (85), 2825–2830.
- (75) Zar, J. Spearman Rank Correlation. In *Encycl Biostat*; 2005; Vol. 5. <https://doi.org/10.1002/0470011815.b2a15150>.